AN INTERFACE MODEL FOR ANALYSIS OF DEFORMATION BEHAVIOUR OF DISCONTINUITIES

Z. MROZ

Institute of Fundamental Technological Research, Polish Academy of Sciences, Swietokrzyska 21, 00-49 Warsaw, Poland

G. GIAMBANCO

Dipartimento di Ingegneria Strutturale e Geotecnica, University of Palermo, Viale delle Scienze, 90128 Palermo, Italy

SUMMARY

An interface constitutive model is presented accounting for slip and sliding effects and also for dilatancy phenomena. The microslip effects are described by considering spherical asperity interaction with variation of contact area and generation of progressive or reverse slip zones. The incremental constitutive equations are derived with proper memory rules accounting for generation and annihilation of particular slip zones during the process of variable loading. It is further assumed that sliding of spherical contacts occurs along large asperities whose slope varies due to the wear process. The predicted shear and dilatancy curves are shown to provide close quantitative simulation of available experimental data. The strain ratchetting effect for non-symmetric cyclic loading was exhibited using the asperity wear model. The model presented could be applied to simulate rock joints, masonry, or concrete cracked interfaces, under monotonic and cyclic loading.

KEY WORDS: interface constitutive model; deformation behaviour; spherical asperity interaction; dual asperity interaction: shear and dilatancy of joints

1. INTRODUCTION

The presence of discontinuties is a common feature of many mechanical systems. We mention here such problems as the structural analysis of a jointed rock mass or of a 'non-virgin' masonry structure where friction sliding and opening along cracked interfaces constitute the main mode of deformation. In recent years, there is a growing attention of structural mechanics researchers to the analysis and modelling of joints regarding them as interfaces between distinct parts of the same structural system. Interface models have been proposed and implemented within the finite element codes by numerous researchers, for instance, Goodman *et al.*,[1] Ghaboussi *et al.*,[2] Plesha,[3] Desai and Ma,[4] Navayogarajah *et al.*,[5] thus providing analysis of complex structural systems.

The idealized constitutive models usually account for the effect of debonding, sliding and dilatancy along discountinuities. Debonding or joint opening occurs when two contacting surfaces separate and form a gap with no interaction forces transmitted. On the other hand, sliding represented by the tangential velocity discontinuity, is usually accompanied by dilatancy or contraction specified by the normal velocity discontinuity. The dilatancy property plays an important role in the analysis of a jointed rock mass and cannot be neglected in view of its stabilizing effect, as emphasized by Goodman and Dubois.[6] The relation of dilatancy effect to roughness of joint surfaces stimulated numerous researchers to apply the wedge asperity model for which two plates slide relatively to each other along asperities thus inducing dilatancy and contraction for reverse sliding. The asperity model first used by Patton[7] to model rock joint was

next extended by Barton *et al.*[8] and Plesha,[9] who considered also surface wear effect on joint response. Snyman and Martin[10] presented a consistent formulation of asperity model in the incremental form using the relative displacement space representation. The study of Michalowski and Mroz[11] of sliding modes along wedge asperities exhibited the non-associated sliding rule for the velocity potential depending on friction coefficient and asperity angle. In the recent work of Mroz and Stupkiewicz[12] the explicit forms of the limit friction conditions and the sliding potential were provided.

The other possibility to simulate the interface response is to apply a phenomenological constitutive model for which the sliding mode is associated with the interface yield condition expressed in terms of contact tractions and interface state variables whose evolution depends on tangential slip and dilatancy. The classical Coulomb or parabolic yield condition combined with a non-associated flow rule is frequently used, cf. Reference 13. For a more accurate interface description with critical state models are applied. Both hardening and softening is assumed to occur depending on the value of normal stress and the critical state corresponds to the tangential slide with no dilatancy, cf. Lofti and Shing[14]. The concept of fully adjusted critical state approach accounting for asperity evolution was presented by Navayogarajah *et al.*[5]

Another important factor is the *microslip effect* occurring before the sliding mode develops at the contact. The slip occurs when the limit friction condition is reached only on a part of contact area, the remaining area constituting a sticking zone. On the other hand, the slide occurs on the whole contact area. In fact, for small relative displacement amplitude, only microslip mode will occur and for cyclic loading the hysteresis loops will be generated thus inducing energy dissipation.

The present work is devoted to an interface constitutive model for which both slide and slip effects will be incorporated into the description. It is assumed that the external limit friction surface will be associated with sliding mode and the internal slip surface translating in the interior of the sliding surface will be associated with sliding mode and the internal slip surface translating in the interior of the sliding surface will be associated with slip effect. The memory of progressive and reverse slip will be introduced into the model by considering the consecutive loading surfaces. The memory of progressive and reverse slip will be introduced into the model by considering the consecutive loading surfaces. The structure of the constitutive model will be similar to that discussed by Jarzebowski and Mroz[15], for the case of microslip and sliding of two spheres under normal and tangential forces. The asperity based simulation of dilatancy and configuration hardening and softening will be applied in specifying the evolution of sliding surface. It is believed that the present model will be applicable to simulation of rock joint or cracked interface in concrete or masonry structures under both monotonic loading inducing fairly large relative displacements and cyclic loading inducing hysteretic effects in slip or sliding regimes. In the next three sections the model description will be presented. In Section 5, the model will be applied to simulate some characteristic deformation response features of joints observed experimentally.

2. GENERAL ASSUMPTIONS

Consider a planar joint surface between two bodies Ω_1 and and Ω_2 as shown in Figure 1(a). Denote by t_1, n_1 the local orthogonal reference system with t_1 tangential and n_1 normal to the joint, pointing in the exterior of Ω_1. The joint can be replaced by contact layer of thickness h. The contact stress components are $\sigma_n = \mathbf{n} \cdot \boldsymbol{\sigma} \mathbf{n}$ and $\boldsymbol{\tau}_n = \boldsymbol{\sigma} - (\mathbf{n} \cdot \boldsymbol{\sigma} \mathbf{n})\mathbf{n}$. For the plane problem, with slip occurring along t_1, only components σ_n and τ_{n1} are considered. The index 1 will be omitted in the subsequent analysis, so $\tau_{n1} = \tau_n$. Obviously, there is continuity of traction components at the interface, so we have

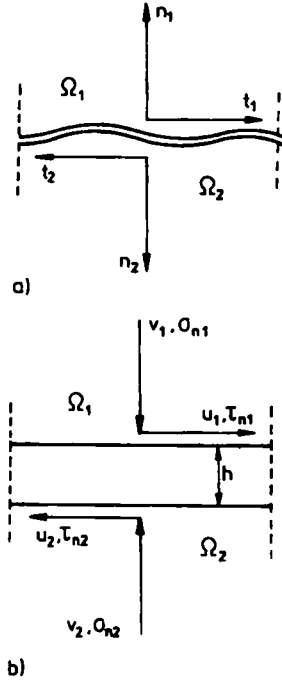$$[\tau_n] = [\tau_{n1}] = 0, \quad [\sigma_n] = 0 \tag{1}$$

Figure 1. (a) Interface between two bodies Ω_1 and Ω_2; (b) interface layer of thickness h between Ω_1 and Ω_2

where [ ] denotes the discontinuity of the enclosed quantity. On the other hand, the displacement components u_1, v_1 and u_2, v_2 of bodies Ω_1 and Ω_2 referred to (t_1, n_1) system at the interface may suffer discontinuity, thus

$$[u] = u_1 - u_2, \qquad [v] = v_1 - v_2 \tag{2}$$

The engineering strain components within the contact layer are specified as follows:

$$\gamma_n = \frac{[u]}{h}, \qquad \varepsilon_n = \frac{[v]}{h} \tag{3}$$

and are assumed as constant within the layer. The following work rate equality holds:

$$\dot{W} = \sigma_n \dot{\varepsilon}_n h + \tau_n \dot{\gamma}_n h = \sigma_n [\dot{v}] + \tau_n [\dot{u}] \tag{4}$$

so σ_n, τ_n and $[u], [v]$ can be regarded as conjugate stresses and strains generating the localized work rate along the interface.

Obviously, γ_n and ε_n are used as measures of slide and dilatancy of the contact layer. The additive decomposition of total strains or displacement discontinuities is assumed, thus

$$\varepsilon = \varepsilon^e + \varepsilon^s \quad \text{or} \quad [u] = [u^e] + [u^s] \tag{5}$$

where ε^e is the elastic strain and ε^s denotes the irreversible strain, similarly $[u^e]$ and $[u^s]$ denote the elastic and sliding or slip displacement. The elastic strain components are related to contact
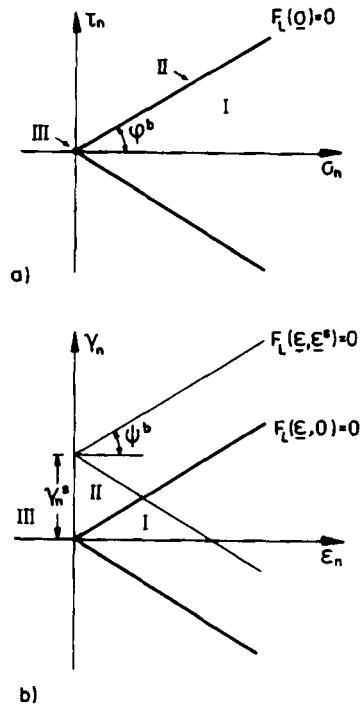
Figure 2. Limit friction condition in (a) the stress plane and (b) strain plane.

stresses by the constitutive law which has the form

$$\boldsymbol{\sigma} = \mathbf{E}^{\mathbf{e}}\boldsymbol{\varepsilon}^{\mathbf{e}} = \frac{1}{h}\,\mathbf{E}^{\mathbf{e}}[\mathbf{u}^{\mathbf{e}}] \tag{6}$$

where

$$\boldsymbol{\sigma} = [\tau_n \;\; \sigma_n]^{\mathrm{T}} \tag{7a}$$

$$\boldsymbol{\varepsilon} = [\gamma_n \;\; \varepsilon_n]^{\mathrm{T}} \tag{7b}$$

$$\mathbf{E}^{\mathbf{e}} = \begin{bmatrix} E_t^e & 0 \\ 0 & E_n^e \end{bmatrix} \tag{7c}$$

and E_t^e, E_n^e denote the tangential and normal stiffness moduli. For the non-linear case, E_t^e, E_n^e are the secant moduli.

The straining of the interface layer is combined with the sliding mode when the limit friction condition is reached. Assuming Coulomb condition, Figure 2(a), in the form

$$F_{\mathrm{L}}(\boldsymbol{\sigma}) = |\tau_n| - \sigma_n \tan \phi^b \leqslant 0 \tag{8}$$

the sliding rule is expressed as follows:

$$\gamma_n^s = \dot{\lambda}\,\mathrm{sgn}(\tau_n), \qquad \dot{\lambda} > 0, \qquad \dot{\lambda}F_{\mathrm{L}} = 0$$

$$\varepsilon_n^s = 0 \tag{9}$$

Here ϕ^{b} denotes the basic friction angle associated with a perfectly smooth contact surface for which the effect of asperities or contact dilatancy is neglected. The friction locus can also be presented in the strain plane by using (6) and (7), namely,

$$\bar{F}_{L}(\varepsilon, \varepsilon^{s}) = E_{t}^{c}|\gamma_{n} - \gamma_{n}^{s}| - E_{n}^{c}(\varepsilon_{n})\tan\phi^{b} \leqslant 0 \tag{10}$$

or

$$\bar{F}_{L}(\varepsilon, \varepsilon^{s}) = |\gamma_{n} - \gamma_{n}^{s}| - (\varepsilon_{n})\tan\psi^{b} \leqslant 0 \tag{11}$$

where $\tan\psi^{b} = (E_{n}^{c}/E_{t}^{c})\tan\phi^{b}$. The compressive stress σ_{n} and the conjugate contractive strain ε_{n} are assumed as positive. Thus, when E_{t}^{c} and E_{n}^{c} are constant, the limit friction locus in the strain space is represented by two straight lines inclined at the angle ψ^{b} to the ε_{n}-axis with the vertex translated along the γ_{n}-axis due to sliding displacement, Figure 2(b). Thus, for the unloading path within the domain $F_{L} < 0$, only elastic strains occur. This simple model will next be generalized by accounting for microslip effects occurring for stress paths within the domain $F_{L} < 0$.

3. CONSTITUTIVE MODEL FOR TABULAR JOINT ACCOUNTING FOR SLIDING AND MICROSLIP EFFECTS

The classical contact friction formulation discussed in the previous section will now be modified by accounting for non-linear elastic contact compliance and also for microslip effects occurring for states within the domain $F_{L} < 0$ so far representing rigid for elastic response. Now, however we shall assume that slip strains develop before reaching the limit friction condition, so we have

$$\dot{\varepsilon} = \dot{\varepsilon}^{e} + \dot{\varepsilon}^{m}, \qquad F_{L}(\sigma) < 0 \text{ or } F_{L}(\sigma) = 0, \qquad \dot{F}_{L}(\sigma) < 0$$

$$\dot{\varepsilon} = \dot{\varepsilon}^{e} + \dot{\varepsilon}^{m} + \dot{\varepsilon}^{s}, \qquad F_{L}(\sigma) = 0, \qquad \dot{F}_{L}(\sigma) = 0 \tag{12}$$

where $\dot{\varepsilon}^{m}$ denotes the microslip strain rate and $\dot{\varepsilon}^{s}$ is the sliding strain rate occurring when the limit friction conditions is reached, $F_{L}(\sigma) = 0$. Referring to Figure 2(b), three modes of contact behaviour can be distinguished. In the domain I, $\bar{F}_{L} < 0$, elastic slip response occurs, whereas in the domain II, $\bar{F}_{L} = 0$, elastic slip, and sliding strains may develop. Finally, in the domain III, contact separation occurs, and $\varepsilon_{n} < 0$, $\sigma_{n} = 0$.

Assume that within the contact interface Π the two bodies Ω_{1} and Ω_{2} interact through spherical asperities. For simplicity, it is assumed that the radii of all asperities are the same and equal R. The contact response can be discussed in considering two typical spheres of equal radii acted on by normal and tangential forces with account for frictional slip at the contact area, Figure 3(a). The classical solution of Mindlin and Deresiewicz,[16] recently reanalysed by Dobry et al.[17] and also by Jarzebowski and Mroz,[15] who derived slip and memory rules for this case, can now be applied. Figure 3(b) presents a more general model where spherical apserities are of different radii with initial gap distribution and only partial contact, varying during compression process with increasing normal stress σ_{n}. This effect will be accounted for later by introducing an exponential parameter in specification of the contact compliance.

The representative element area within Π can now be assumed as a square $2R \times 2R$ containing one spherical asperity cross-section, cf. Figure 3(c). The normal and tangential forces carried through this area equal

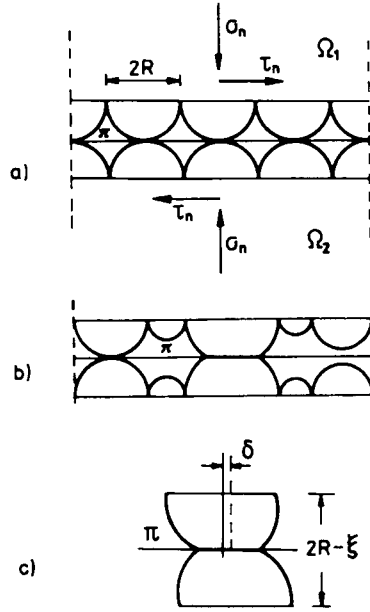$$N = \sigma_{n}4R^{2}, \qquad T = \tau_{n}4R^{2} \tag{13}$$

Figure 3. (a) Asperity model of the interface with simultaneous contact; (b) Asperity model with initial gap distribution. (c) Normal and tangential compliance at the contact of two spheres

The contact area radius a equals:

$$a = (k \cdot N \cdot R)^{1/3} \tag{14}$$

where $k = 3(1 - v^2)/4E$, further E and v denote Young modulus and Poisson ratio. In view of (13) and (14), there is

$$\beta = \frac{a}{R} = (4k\sigma_n)^{1/3}, \quad \sigma_n > 0 \tag{15}$$

where the contact factor β provides a measure of the actual contact area with respect to the nominal area within the plane Π. In fact, the area ratio equals $\pi\beta^2$. Due to the normal load N, the two spherical asperities are approaching by

$$\xi = 2\left(\frac{kN}{R^{1/2}}\right)^{2/3} \tag{16}$$

Denoting by $\varepsilon_n = \xi/2R$ the non-dimensional normal displacement, we have

$$\varepsilon_n = (4k\sigma_n)^{2/3} \tag{17}$$

The normal elastic compliance for two semi-spheres equals:

$$D_n^e = \frac{d\varepsilon_n}{d\sigma_n} = \frac{1 - v}{G\beta} \tag{18}$$

where G denotes the shear modulus. The tangential load T produces a relative displacement δ of the centres of spheres with respect to the uniform displacement of the adhered portion provided by

$$\delta = \frac{3(2-v)\tan\phi^b N}{16Ga}\left[1 - \left(1 - \frac{T}{\tan\phi^b N}\right)^{2/3}\right] \tag{19}$$

Denoting by $\gamma_n = \delta/R$ the non-dimensional slip and using (13) and (15), we have

$$\gamma_n = \frac{3(2-v)\tan\phi^b\sigma_n}{4\beta G}\left[1 - \left(1 - \frac{\tau_n}{\tan\phi^b\sigma_n}\right)^{2/3}\right] \tag{20}$$

The tangential compliance can now be specified from (20):

$$D_t = \frac{d\gamma_n}{d\tau_n} = \frac{2-v}{2\beta G}\left(1 - \frac{\tau_n}{\tan\phi^b\sigma_n}\right)^{-1/3} \tag{21}$$

The elastic tangential compliance can be defined as the value of D_t for $\tau_n = 0$, thus

$$D_t^e = \frac{2-v}{2\beta G} \tag{22}$$

The elastic stiffness matrix is now specified as follows:

$$\mathbf{E} = \begin{bmatrix} \dfrac{1}{D_t^e} & 0 \\ 0 & \dfrac{1}{D_n^e} \end{bmatrix} \tag{23}$$

Let us note that though D_t^e and D_n^e depend on the contact radius and hence on normal stress, their ratio is constant. In fact, in view of (18) and (22), we have

$$\frac{E_n^e}{E_t^e} = \frac{D_t^e}{D_n^e} = \frac{(2-v)}{2(1-v)} \tag{24}$$

Application of the tangential stress τ_n induces development of slip within a ring domain (called microslip zone) expanding from the outer contact boundary. The interior ring radius c specifying the central sticking zone is determined from the formula

$$c = a\left(1 - \frac{\tau_n}{\tan\phi^b\sigma_n}\right)^{1/3} \tag{25}$$

A measure of the sticking area with respect to the contact area is provided by the non-dimensional parameter

$$\zeta = \frac{c}{a} = \left(1 - \frac{\tau_n}{\tan\phi^b\sigma_n}\right)^{1/3} \tag{26}$$

Thus for $\tau_n = 0$ there is $\zeta = 1$ and no slip occurs. On the other hand, when $\tau_n = \sigma_n\tan\phi^b$, then $\zeta = 0$ and the slip zone coincides with the contact zone. The sliding mode then initiates at the contact.

3.1. Description of the microslip response at the interface

Using the spherical asperity model briefly specified by equations (13)–(26) and following the previous treatment by Jarzebowski and Mroz,[15] let us discuss the particular loading events induced by varying normal and tangential tractions within the domain $F_L(\sigma) < 0$. The characteristic phenomena during such loading are: (i) the varying contact area due to varying normal compression, (ii) development of consecutive slip zones for varying tangential traction, (iii) simultaneous variation of contact area and evolution of slip zones for combined action of normal and tangential tractions. The variation of contact area is a fully reversible phenomenon occurring for any traction oriented at an angle less than ϕ^b with respect to normal direction. The contact area variation will be represented by an *elastic surface* $F_0 = 0$ translating with the stress point in the σ_n, τ_n-plane. On the other hand, the development of slip zones due to varying tangential traction is an irreversible process since when load orientation is reversed, a new reverse slip zone starts to propagate from the contact boundary and interacts with a prior microslip. The effect of prior slip is erased by the consecutive progressing slip when the consecutive zone penetrates through the whole area of prior slip. Finally, for the combined loading of normal and tangential tractions with the traction vector inclined at an angle greater than ϕ^b with respect to the contact normal, both contact area variation and development of microslip zones occur. To represent geometrically these effects in the plane σ_n, τ_n, let us introduce, besides the elastic surface, also the *active slip* and *slip memory surfaces*. It is clear that the active slip surface represents the progressive slip zone and the memory surfaces represent the prior zones whose radii do not vary.

Consider, for instance, the loading program O–A–B–C–D–E consisting of the initial normal compression along OA with subsequent paths AB, BC, CD, DE constituting loading unloading and reloading events in combined normal and tangential loading, Figure 4. For the initial compression OA the contact radius grows with no slip generated. The loading path OA is associated with the angular domain $F_0 \leqslant 0$, represented with the dashed lines in Figure 4(a), sliding along OA with its vertex at the loading point A. The lines $F_0 = 0$ specify the elastic locus associated with variation of contact area. In fact, for any stress increment directed in the interior of the domain $F_0 \leqslant 0$, no finite slip zone is developed and no dissipation is generated, but only the contact area changes. Consider now the loading path AB directed in the exterior of $F_0 = 0$, Figure 4(a). Following AB, the finite slip zone develops at the external contact perimeter. The elastic locus translates so that its vertex coincides with the stress point. Thus at B, this locus is specified by the equation

$$F_0(\sigma_n, \sigma_{nB}) = |\tau_n - \tau_B| - (\sigma_n - \sigma_{nB})\tan \phi^b = 0 \tag{27}$$

Besides the *elastic* locus, let us introduce the *active slip* locus $F_1 = 0$ constituted by two lines parallel to the limit surface lines and interesecting on the σ_n-axis at $(\sigma_{n1}, 0)$, thus

$$F_1(\sigma_n, \tau_n, \sigma_{n1}) = |\tau_n| - (\sigma_n - \sigma_{n1})\tan \phi^b = 0 \tag{28}$$

where

$$\sigma_n = \sigma_n \left(\frac{c_1}{a_1}\right)^3 = \frac{1}{4k}\left(\frac{c_1}{R}\right)^3 \tag{29}$$

Regarding τ_n, σ_n as the external load parameters, it is seen that the active slip locus $F_1 = 0$ and the elastic locus $F_0 = 0$ specify in the stress plane I three zones of incremental contact response at B. When the stress increment is directed into the interior domain I_a of $F_0 = 0$, that is
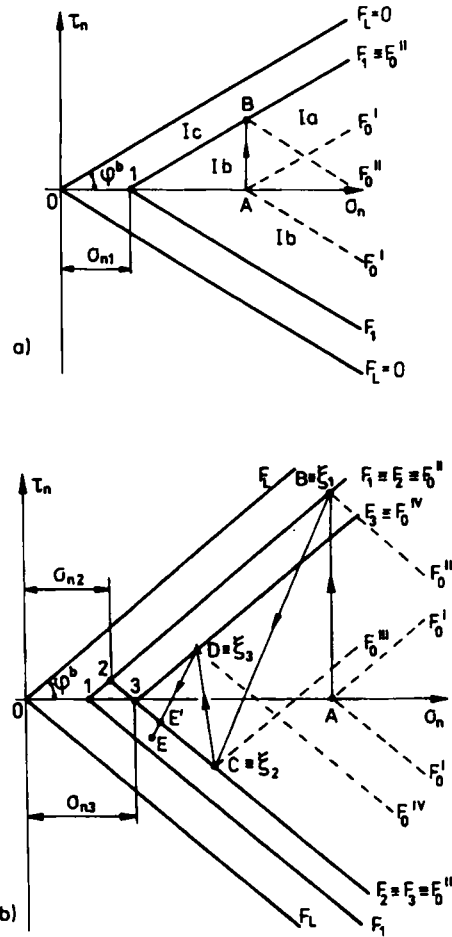
Figure 4. (a) Elastic, limit friction and first active slip locus $F_0 = 0$, $F_L = 0$ and $F_1 = 0$. (b) Active slip and slip memory loci for cyclic shear program O-A-B-C-D-E.

$\dot{\tau}_n - \dot{\sigma}_n \tan \phi^b < 0$, $\dot{\tau}_n + \dot{\sigma}_n \tan \phi^b < 0$, then the contact response is elastic. When the stress increment is directed in the interior of $F_1 = 0$ and exterior of $F_0 = 0$ (domain I_b), that is $\dot{\tau}_n - \dot{\sigma}_n \tan \phi^b < 0$, $\dot{\tau}_n + \dot{\sigma}_n \tan \phi^b > 0$, unloading event, a reverse slip zone will develop from the perimeter of the contact zone. Finally, when the stress increment is directed in the exterior of the loading surface $F_1 = 0$ (domain I_c), so that $|\dot{\tau}_n| - \dot{\sigma}_n \tan \phi^b > 0$, loading event, there is a progressive evolution of the initial slip zone and the loading surface $F_1 = 0$ will further be translating along the σ_n-axis.

When the stress increment at B is directed into the unloading domain I_b, Figure 4(b), the active loading locus $F_1 = 0$ becomes the *first memory locus* with the associated slip zone radius c_1 fixed. This memory locus is identified by the *stress reversal* (or *stress reference*) point ζ_1 corresponding to the stress state B. A set of unloading loci $F_2 = 0$ are generated, starting from the initial configuration coinciding at B with the elastic locus $F_0 = 0$. In the contact plane the reverse slip

zone starts to propagate from the contact perimeter. The associated unloading locus $F_2 = 0$ is composed of two lines with the vertex 2 sliding along the side $1 - B$ of the memory locus. The value σ_{n2} at the vertex is directly related to the size of the reverse slip zone $r = c_2$, thus

$$c_2 = R[4k\sigma_{n2}]^{1/3} \tag{30}$$

The elastic locus $F_0 = 0$ is translated with the stress point to C, thus specifying three zones of incremental loading from C, similarly to the zones at B. Along CD, the reloading process starts with a new reloading locus $F_3 = 0$ generated with its vertex 3 sliding along the side 2-C of the previous locus which now becomes the *second memory locus*. This second surface is defined by the reference points ξ_1 and $\xi_2 \equiv C$. The vertex σ_{n3} of $F_3 = 0$ is related to the size of the reloading slip zone c_3 evolving from the contact perimeter, so that

$$c_3 = R[4k\sigma_{n3}]^{1/3} \tag{31}$$

Referring to Figure 4(b), it is seen that the prior active slip surface becomes the memory surface when the respective loading, unloading, and reloading events follow each other. Therefore, the set of stress reversal points which have been collected, define together with the actual stress state, the loading history and provide a full description of the slip phenomenon. The number of reversal points stored in the memory can also decrease during the process. For instance, along the stress path DE, when the actual stress state reaches the surface $F_2 = 0$, at E', the reverse slip that arises along DE' erases the slip developed in the path CD. The path E'E corresponds to unloading event from B and the reversal points ξ_2 and ξ_3 are deleted. The only reference point ξ_1, associated to the surface $F_1 = 0$ is stored in the memory, in the alternating slip process. Let us note that when the stress point reaches the first memory surface, the reverse slip erases the slip generated along AB, thus erasing the reference point ξ_1.

Let us now present the incremental relations for particular slip events. Consider first the loading program AB for which the slip zone starts to propagate from the external contact perimeter. In view of (18) and (19) we have

$$\begin{bmatrix} \dot{\gamma}_n \\ \dot{\varepsilon}_n \end{bmatrix} = \begin{bmatrix} \dfrac{2-\nu}{2G\beta}\dfrac{a_1}{c_1} & \dfrac{2-\nu}{2G\beta}\tan\phi^b\left(1-\dfrac{a_1}{c_1}\right) \\ 0 & \dfrac{1-\nu}{G\beta} \end{bmatrix} \begin{bmatrix} \dot{\tau}_n \\ \dot{\sigma}_n \end{bmatrix} \tag{32}$$

the inverse relations, associated with condition $|\dot{\gamma}_n| - \dot{\varepsilon}_n \tan\psi^b > 0$, are

$$\begin{bmatrix} \dot{\tau}_n \\ \dot{\sigma}_n \end{bmatrix} = \begin{bmatrix} \dfrac{2G\beta}{2-\nu}\dfrac{c_1}{a_1} & \dfrac{2G\beta}{1-\nu}\tan\phi^b\left(1-\dfrac{c_1}{a_1}\right) \\ 0 & \dfrac{G\beta}{1-\nu} \end{bmatrix} \begin{bmatrix} \dot{\gamma}_n \\ \dot{\varepsilon}_n \end{bmatrix} \tag{33}$$

Consider now the reverse slip developed for the unloading event BC. A new contact area of radius a_2 and a reverse slip zone of internal radius c_2 occur. The incremental relation

now are

$$\begin{bmatrix} \dot{\tau}_n \\ \dot{\sigma}_n \end{bmatrix} = \begin{bmatrix} \dfrac{2G\beta}{2-v}\dfrac{c_2}{a_2} & \dfrac{-2G\beta}{1-v}\tan\phi^b\left(1-\dfrac{c_2}{a_2}\right) \\ 0 & \dfrac{G\beta}{1-v} \end{bmatrix} \begin{bmatrix} \dot{\gamma}_n \\ \dot{\varepsilon}_n \end{bmatrix} \qquad (34)$$

and the unloading condition is: $\dot{\gamma}_n - \dot{\varepsilon}_n \tan\psi^b < 0$, $\dot{\gamma}_n + \dot{\varepsilon}_n \tan\psi^b > 0$.

When at C the stress path is reversed and directed along CD in the interior of the actual loading surface $F_2 = 0$, the reloading process develops with a new slip zone of internal radius $r = c_3$ generated from the boundary of the new contact area of radius a_3. The stress point remains on the active loading surface $F_3 = 0$, with its vertex 3 specifying the size of the active slip zone by (31). The incremental relation are analogous to (33) with a_3 and c_3 replacing a_1 and c_1. The value of c_i/a_i for $i = 1, 2, 3$ are specified from relations (15) and (25)

$$\frac{c_i}{a_i} = \left(\frac{\sigma_{ni}}{\sigma_n}\right)^{1/3} \qquad (35)$$

Referring to the stress plane, formula (35) can be replaced by

$$\frac{c_i}{a_i} = \left(1 - \frac{\tan\vartheta_i}{\tan\phi^b}\right)^{1/3} \qquad (36)$$

where angle ϑ_i is identified by the vertex of the actual loading surface and by the actual stress state as presented in Figure 5 for the loading, unloading and reloading events.

The incremental relations can now be briefly written for any loading event, namely

$$\dot{\sigma} = \mathbf{E}^*\varepsilon \qquad (37)$$

where

$$E^* = \begin{bmatrix} E_{tt} & E_{tn} \\ 0 & E_{nn} \end{bmatrix} \qquad (38)$$

with

$$E_{tt} = \frac{2G\beta}{2-v}\left(1 - \frac{\tan\theta}{\tan\phi^b}\right)^{p/3} \qquad (39a)$$

$$E_{tn} = \pm\frac{2G\beta}{1-v}\left[1 - \left(1 - \frac{\tan\theta}{\tan\phi^b}\right)^{p/3}\right] \qquad (39b)$$

$$E_{nn} = \frac{G\beta}{1-v}; \qquad (39c)$$

the plus sign being used for loading or reloading events and the minus sign applies for the unloading events.

In presenting (37), (39a)–(39c), we introduce the exponent p in the expressions for stiffness moduli. When $p = 1$, the elastic sphere interaction model is obtained. However, for varying p, we may obtain softer or stiffer slip response resulting in varying dissipation for cyclic straining. Here
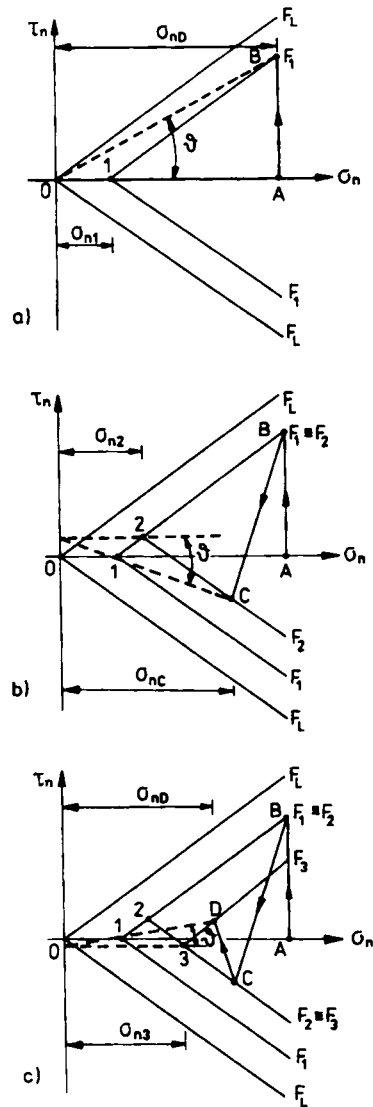
Figure 5. Active surfaces and parameter ϑ identification for (a) loading, (b) unloading and (c) reloading

p can be regarded as an additional structure parameter affecting tangential stiffness of the contact. Thus a more complex asperity interaction with initial gap distribution, Figure 3(b), can be incorporated by selecting a proper value of p.

The microslip process can also be represented in the strain space. In fact, the inelastic strain rate can be decomposed into two parts, that is slip and sliding rates

$$\dot{\varepsilon}^p = \dot{\varepsilon}^m + \dot{\varepsilon}^s, \qquad \dot{\varepsilon} = \dot{\varepsilon}^e + \dot{\varepsilon}^m + \dot{\varepsilon}^s \tag{40}$$
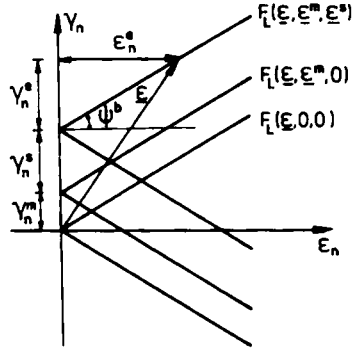
Figure 6. Limit friction conditions in the strain plane

When $F_L(\sigma) < 0$, the sliding strain rate vanishes, $\dot{\varepsilon}^s = 0$. Using (6) and (38), we have

$$\dot{\varepsilon}^e = (E^e)^{-1}\dot{\sigma} = (E^e)^{-1}E^*\dot{\varepsilon} \tag{41}$$

and the slip strain rate is related to the total strain rate as follows:

$$\dot{\varepsilon}^m = \dot{\varepsilon} - \dot{\varepsilon}^e = (I - E^{e^{-1}}E^*)\dot{\varepsilon} \tag{42}$$

where I denotes the unit matrix. In particular, the value of inelastic shear strain rate can be expressed in terms of the components of the total strain rate, namely,

$$\dot{\gamma}_n^m = \left[1 - \left(1 - \frac{\tan\theta}{\tan\phi^b}\right)^{1/3}\right](\dot{\gamma}_n \pm \dot{\varepsilon}_n \tan\psi^b) \tag{43}$$

where the minus sign applies for loading and reloading events and the plus sign applies for unloading events.

In the strain space, the limit friction condition is translated along the γ_n-axis by the amount of the slip strain, thus

$$\bar{F}_L(\varepsilon, \varepsilon^m) = |\gamma_n - \gamma_n^m| - \varepsilon_n \tan\psi^b = 0 \tag{44}$$

where, in view of (24), the angle ψ^b is constant for the case of contact of two spheres.

Similarly, the elastic locus and the active slip surfaces are translated along the γ_n-axis by the amount of slip strain, Figure 6.

3.2. Sliding response at the interface

The sliding strain occurs when the limit friction condition (8) is reacdhed. The non-associated flow rule can now be used

$$\dot{\varepsilon}^s = \begin{cases} 0 & \text{when } F_L(\sigma) \leqslant 0 \text{ or } F_L(\sigma) = 0, \ \dot{F}_L(\sigma) < 0 \\ \lambda \dfrac{\partial G}{\partial \sigma} & \text{when } F_L(\sigma) = 0, \ \dot{F}_L(\sigma) = 0 \end{cases} \tag{45}$$

where $\lambda > 0$ and $G = |\tau|$ is the sliding potential. Alternatively, the limit friction locus can be presented in the strain plane γ_n, ε_n, namely

$$\bar{F}_{\rm L}(\varepsilon, \varepsilon^m, \varepsilon^s) = |\gamma_n - \gamma_n^s - \gamma_n^m| - \varepsilon_n \tan \psi^b = 0 \tag{46}$$

and is translated through the distance $\gamma_n^s + \gamma_n^m$ along the γ_n-axis, Figure 6.

4. SLIP AND SLIDING ALONG ASPERITIES

So far, we have assumed the slip and sliding to occur within the plane of tabular interface. The contact area represented the varying configuration affecting both normal and tangential compliance. However, the other important configuration variable can be introduced by assuming the slip phenomena to occur along the inclined plane representing the large local asperity. In other words, the contact interface is assumed to be composed as asperities of two different size scales: *small-* or *high-order* asperities represented by contacting spheres, and *large* or *primary asperities*, represented by curvilinear, periodically repeated profile, including dilatancy and additional hardening or softening at the interface.

The effect of roughness on the joint response was treated by numerous authors. Experimental evidence and analytical or numerical treatments indicate that this effect plays an important role in generating shear strength and dilatancy. In particular, when sliding occurs along the plane inclined at the angle α to the nominal interface plane, Figure 7, the shear stress equals

$$\tau_n = \sigma_n \tan (\phi^b \pm \alpha) \tag{47}$$

and for varying $\alpha(s)$ (where s is the length of contact line) there is

$$\frac{{\rm d}\tau_n}{{\rm d}s} = \pm \frac{\sigma_n}{\cos^2(\phi^b + \alpha)} \frac{{\rm d}\alpha}{{\rm d}s} \tag{48}$$

where the plus sign applies to the case of sliding upward the asperity and the minus sign corresponds to the case of downward sliding. From (48) it is easy to see that for upward sliding there is *configuration* (or *curvature*) *hardening* ($\tau_n > 0$, ${\rm d}\tau_n > 0$ for ${\rm d}\alpha > 0$) for the concave asperity shape and *configuration* (or *curvature*) *softening* ($\tau_n > 0$, ${\rm d}\tau_n < 0$ for ${\rm d}\alpha < 0$) for the convex asperity shape. On the other hand, for downward sliding, there is configuration softening ($\tau_n < 0$, ${\rm d}\tau_n > 0$ for ${\rm d}\alpha < 0$) for concave asperity and hardening ($\tau_n < 0$, ${\rm d}\tau_n < 0$ for ${\rm d}\alpha > 0$) for convex asperity.

The most widely used model is the saw-tooth asperity model, Figure 8(a), for which α represents the average measure of roughness. Patton[7] was the first to apply this model to predict shear strength of rock joints. In the study of Barton *et al.*,[8] the value of α is related to geometrical features of contact planes, mechanical properties of materials constituting two bodies in contact, and the actual stress state. Plesha[9] adopted the Patton[7] model also to describe the dilatant property of the joint. The discontinuity was assumed to be initially full seated with no void space. When sliding occurs, only the left-hand or right-hand side of the asperities are in contact. The sliding strain and dilatancy are thus coupled through the asperity shape. In the same paper, the author considered also a curvilinear asperity model assuming the sinusoidal shape for which the slope varies with the tangential displacement. Biaxial sliding rules for wedge shaded asperities were studied by Michalowski and Mroz,[11] who demonstrated that such rules are not associated by the normality property with the limit friction condition. An interface element based on the asperity model in describing the dilatant behaviour was presented by Snyman and Martin,[10] who assumed a logarithmic spiral to model the asperity shape.
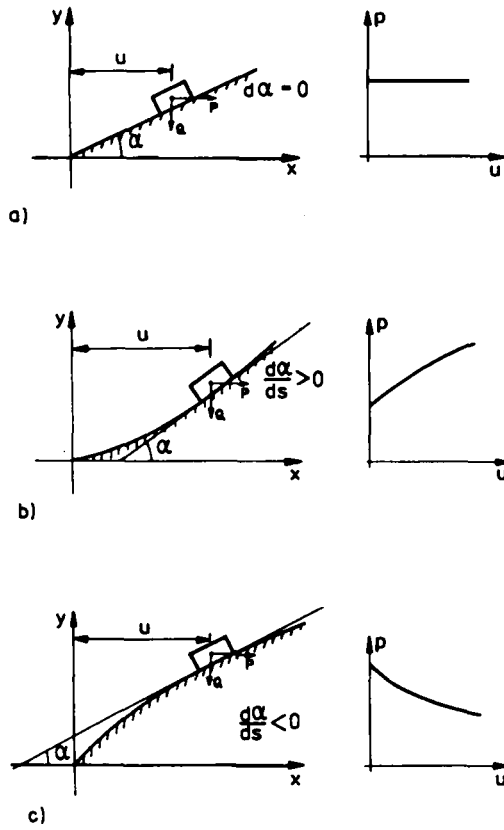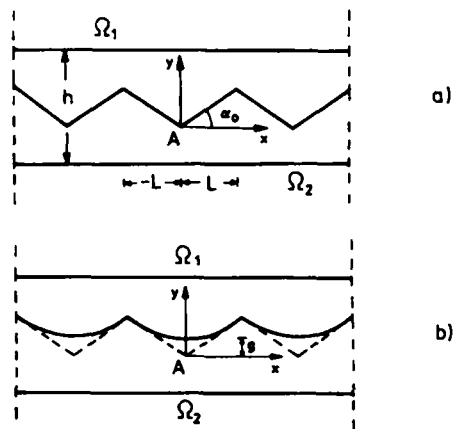
Figure 7. Effects of large asperities on joint response

Figure 8. (a) Saw-tooth asperity model; (b) proposd asperity model

In the present work, we assume that the initial sawtooth shape, Figure 8(a), changes due to wear process. Locate the local co-ordinate system x, y at the vertex of the upper body asperity, Figure 8(b). The initial asperity shape is described in this system by the function $|y_0| = \tan \alpha_0 x$ or $|\bar{y}_0| = \tan \alpha_0 \gamma$, where $\bar{y} = y/h$ and $\gamma = x/h$ are non-dimensional co-ordinates referred to the interface thickness. Introduce the measure of the wear $g(W_f)$ which specifies the shape of asperity, namely

$$\bar{y} = f(\gamma) = (\tan^2 \alpha_0 \gamma^2 + g^2)^{1/2} \tag{49}$$

which corresponds to a hyperbola having the principal axis coinciding with the y-axis and the asymptotes $y = \pm \tan \alpha_0 \gamma$. The slope α of (47) is now specified from (49), thus

$$\alpha(\gamma) = \arctan \left[\frac{\tan^2 \alpha_0 \gamma}{(\tan^2 \alpha_0 \gamma^2 + g^2)^{1/2}} \right] \tag{50}$$

The value of the wear function specifies the actual asperity shape. In particular, for $g = 0$, we have the initial wedge shaped asperity $\bar{y} = \bar{y}_0 = \tan \alpha_0 \gamma$ and for $g \to \infty$ there is $\alpha \to 0$, that is the asperity, passes into the flat plane. Similarly to Plesha[9] assumption, the evolution of the damage function is specified in the form

$$g(W_f) = g^f(1 - e^{W_f/W_0}) \tag{51}$$

where W_f is the specific friction work of tangential contact stress

$$W_f = h \int_0^t \tau_n \dot{\gamma}_n^p \, dt = \int_0^t \tau_n [\dot{u}^p] \, dt \tag{52}$$

and the inelastic strain is composed of microslip and sliding strains. The parameter W_0 has the dimension of work specifying the rate of wear and g^f is the asymptotic value of g.

The incremental relations for sliding strain are now presented as follows. Considering the limit friction condition in the form

$$F_L(\tau_n, \sigma_n, \alpha) = |\tau_n| - \sigma_n \tan(\phi^b + \alpha) = 0 \tag{53}$$

we have the non-associated sliding rule

$$\dot{\gamma}_n^s = \dot{\gamma}, \qquad \dot{\varepsilon}_n^s = \dot{\gamma} \tan \alpha, \qquad \dot{\gamma} > 0 \tag{54}$$

Assume the asperity angle to be specified by the function $\alpha = \alpha(\gamma)$. The consistency condition imposed on (53) then provides

$$\dot{\gamma} = \frac{\dot{\tau}_n - \tan(\phi^b + \alpha)\dot{\sigma}_n}{\alpha'} > 0 \tag{55}$$

where $\alpha' = d\alpha/ds$. Obviously, for the case of configuration hardening in view of (55) there is, $\alpha' > 0$, $\dot{\tau}_n - \tan(\phi^b + \alpha)\dot{\sigma}_n > 0$, and

$$\begin{bmatrix} \dot{\gamma}_n^s \\ \dot{\varepsilon}_n^s \end{bmatrix} = \frac{1}{\alpha'} \begin{bmatrix} 1 & -\tan(\phi^b + \alpha) \\ -\tan \alpha & \tan(\phi^b + \alpha)\tan \alpha \end{bmatrix} \begin{bmatrix} \dot{\tau}_n \\ \dot{\sigma}_n \end{bmatrix} \tag{56}$$

4.1. Derivation of incremental slip rules

Consider now the incremental slip along the large asperity inclined at the angle α to the nominal plane, Figure 9. Introduce the local co-ordinate system t^*, n^* and denote by τ_n^*, σ_n^* the
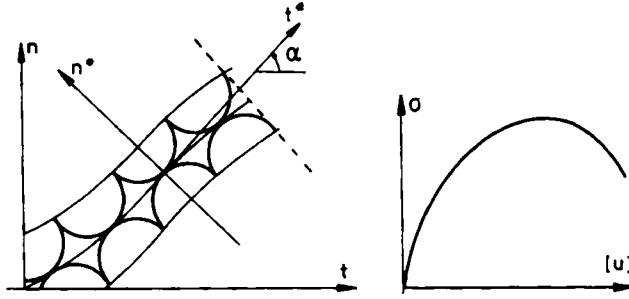
Figure 9. Coupled model of small and large asperities

contact stress components in this system, with the conjugate slip strain rates $\dot{\gamma}_n^*, \dot{\varepsilon}_n^*$. Assuming the contact to occur on spherical asperities of the second order, the slip rule (37) can be written in the local system

$$\dot{\sigma}^* = E^* \dot{\varepsilon}^* \qquad (57)$$

where the matrix E^* is specified by (38) and (39) for different loading events. Let us refer the stress and strain rate states to the nominal reference system t, n. We have

$$\sigma = R^T \sigma^* \qquad (58a)$$

$$\dot{\varepsilon} = R^T \dot{\varepsilon}^* \qquad (58b)$$

where R is the orthogonal rotation matrix. From (54) it follows that

$$\dot{\sigma} = \dot{R}^T \sigma^* + R^T \dot{\sigma}^* \qquad (59)$$

and using equation (57), we have

$$\dot{\sigma} = \dot{R}^T R \sigma + R^T E^* \dot{\varepsilon}^* = \dot{R}^T R \sigma + R^T E^* R \dot{\varepsilon} = \omega \sigma + E \dot{\varepsilon} \qquad (60)$$

where

$$\omega = \dot{R}^T R, \qquad E = R^T E^* R \qquad (61)$$

and ω is the relative spin of axes of two systems, E denotes the tangential matrix transformed to t, n system. Noting that

$$R = \begin{bmatrix} \cos \alpha & -\sin \alpha \\ \sin \alpha & \cos \alpha \end{bmatrix} \qquad (62a)$$

$$\omega = \dot{R}^T R = \begin{bmatrix} 0 & 1 \\ -1 & 0 \end{bmatrix} \dot{\alpha} \qquad (62b)$$

$$E = \begin{bmatrix} E_{tt} & E_{tn} \\ 0 & E_{nn} \end{bmatrix} \qquad (62c)$$

$$\dot{\alpha} = \alpha' \dot{\gamma}_n^* = \alpha' (\dot{\gamma}_n \cos \alpha - \dot{\varepsilon}_n \sin \alpha) \qquad (62d)$$

we obtain the explicit form of (60), namely,

$$\begin{bmatrix} \dot{t}_n \\ \dot{\sigma}_n \end{bmatrix} = \begin{bmatrix} A_{tt} & A_{tn} \\ A_{nt} & A_{nn} \end{bmatrix} \begin{bmatrix} \dot{\gamma}_n \\ \dot{\varepsilon}_n \end{bmatrix} \tag{63}$$

where

$$A_{tt} = E_{tt}\cos^2\alpha + E_{tn}\cos\alpha\sin\alpha + E_{nn}\sin^2\alpha + \sigma_n\cos\alpha\alpha'$$

$$A_{tn} = -E_{tt}\sin\alpha\cos\alpha + E_{tn}\cos^2\alpha + E_{nn}\sin\alpha\cos\alpha - \sigma_n\sin\alpha\alpha'$$

$$\tag{64}$$

$$A_{nt} = -E_{tt}\sin\alpha\cos\alpha - E_{tn}\sin^2\alpha + E_{nn}\sin\alpha\cos\alpha - \tau_n\sin\alpha\alpha'$$

$$A_{nn} = E_{tt}\sin^2\alpha - E_{tn}\sin\alpha\cos\alpha + E_{nn}\cos^2\alpha + \tau_n\sin\alpha\alpha'$$

and E_{tt}, E_{tn}, E_{nn} are specified by (39a)–(39c)

5. NUMERICAL EXAMPLES

A number of examples are now presented in order to illustrate the predictions of the proposed model and compare them with other numerical results and experimental data. The constitutive model developed in the previous section is here implemented in order to simulate analytically, direct shear tests on specimens with an internal discontinuity. The monotonic and cyclic tests are performed using the equations already discussed with the exception that in the case of cyclic tests, equation (50), describing the asperity evolution, is replaced by

$$\alpha(\gamma)_k = \arctan\left[\frac{\tan^2(\alpha_k)_0\gamma}{(\tan^2(\alpha_k)_0\gamma^2 + g_k^2}\right], \quad k = 1, 2 \tag{65}$$

where subscript $k = 1$ if the right-hand side of the asperity is active or $k = 2$ if the left side is active. Thus in the following, different initial angles for the two sides can be considered and also it is assumed that each surface of the irregularity degrades independently.

In the first example a monotonic shear test is analysed to illustrate the performance of the model in reproducing the actual behaviour of a rock joint. The effects connected with the introduction of primary and second-order asperities are discussed. In the second example, a particular attention is paid to the primary asperity model. The results reported in terms of shear stress, shear strain and dilatancy for the case of cyclic test are compared with model predictions. In the third example, the classical experimental results obtained by Kutter and Weissbach[19] are compared with the model prediction and the evolution of the contact surface during the three cycles can be analysed. Finally, in the fourth example, it is shown how the microslip henomena can affect the global behaviour of a joint which has been analysed experimentally by Jing.[20]

5.1. Example 1. Monotonic shear with different normal stress

In this example, the present model, is applied to simulate a laboratory direct shear test at various levels of constant compressive stress. In order to compare the model prediction with the experimental data, the shear test conducted on an artificial joint by Barton et al.[18] has been chosen. The specimen in a form of square block of dimensions 250×250 mm tested experimentally is subjected to a constant normal stress of $\sigma_n = 0.09$ MPa and to a monotonically
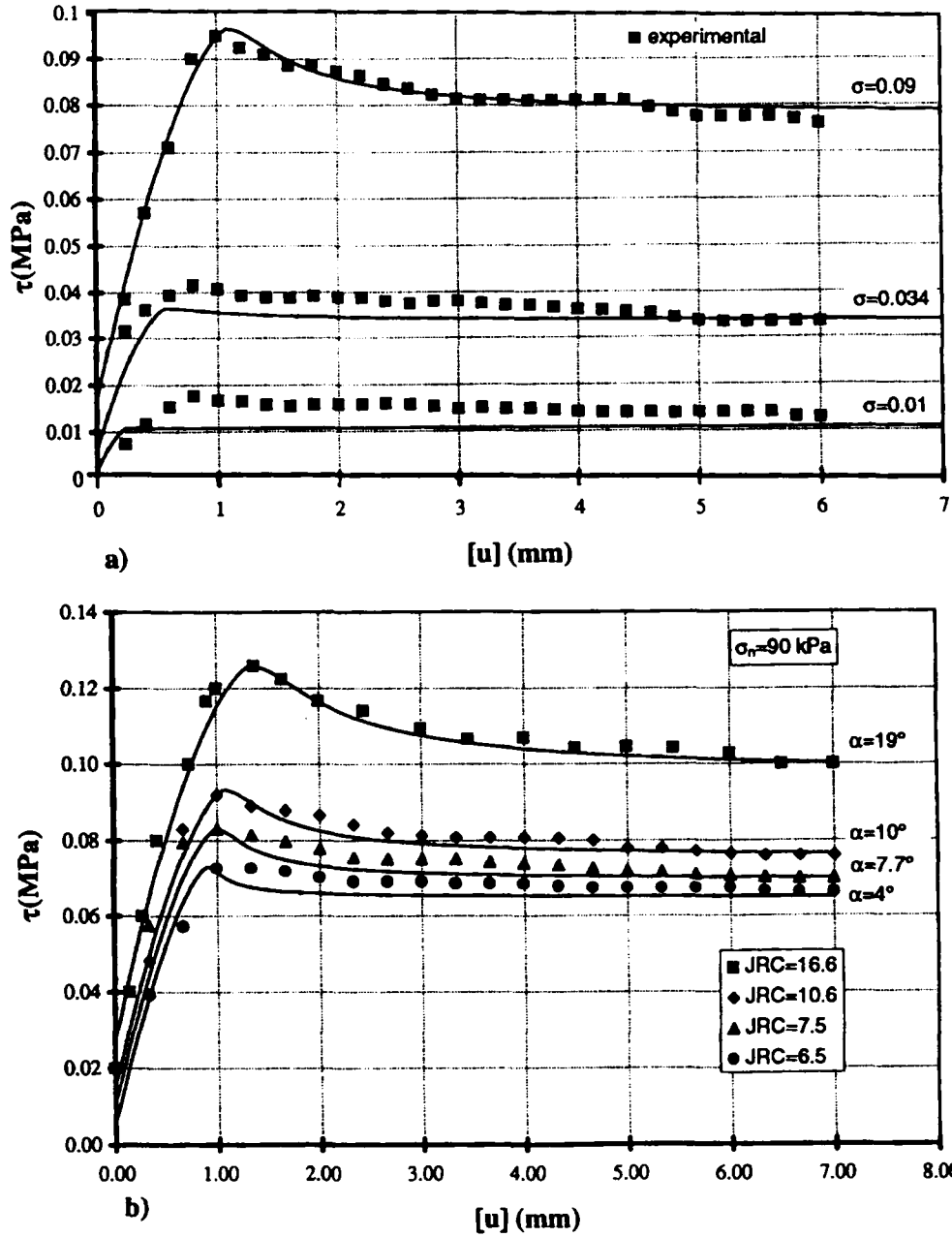
Figure 10. Results for the simulation of Bandis' direct shear test

increasing tangential displacement reaching 7 mm. The obtained results, reported in Figure 10(a), show the pre-peak stage characterized by a non-linearity of the shear curve and a softening stage starting at the stress peak has been adopted and the following elastic moduli have been used: $E = 8$ MPa, $v = = 0.35$. The initial shape of the asperities and their evolution is described by

equations (50) and (51), assuming the following values of the parameters: $\phi^b = 35°$, $\alpha_0 = 19°$, $g^f = 30$, $W_0 = 0.5$ kN cm.

The comparison between theoretical and experimental results indicate that the model describes well the deformation response of the joint in the tangential direction under monotonic load. The microslip effects, when accounted for, provide a non-linear behaviour in the pre-peak stage. Until now this non-linearity was associated with the variation of the shear modulus with the shear displacement and was modelled by formulating empirical work-hardening laws. The post-peak portion predicted by the model provides accurate description of the experimental curve and softening response is associated only with the degradation of primary asperities due to friction dissipation produced during sliding. Besides the predictions obtained for decreasing normal stress ($\sigma_n = 0.034$ and 0.01 MPa), obtained for the same parameter values, provide good correlation with experimental data and illustrate two features also noted in the experiments: the first is the dependence of the shear stiffness on the normal stress. The second feature of softening behaviour is associated with its dependence on the normal stress as the wear of asperities is more pronounced for high values of compressive stress and becomes negligible for low values. Figure 10(b) presents the study of the effect of the initial roughness represented by the varying asperity angle α, with constant normal pressure $\sigma_n = 0.09$ MPa. The experimental data obtained by Barton et al.[18] are also shown in the figure.

5.2. Example 2. Study of the sliding response during cyclic shear loading

The main purpose of this example is to analyse the behaviour of a rough discontinuity under cyclic loading using the proposed asperity model. In this case the microslip effects are not considered and in the pre-peak stage the joint has linear and elastic properties. The model is applied to simulate the direct shear test on a rock specimen 100 mm long and 40 mm thick with a discontinuity, initially fully seated, which crosses the rock in the longitudinal direction dividing it in two blocks. The normal load applied consists of a uniform vertical pressure of 90 KPa and is maintained constant during the shear test. Simulation has been performed using an interface model of thickness $h = 4$ mm of the specimen and with the following material properties: $E = 1000$ KPa, $v = 0.3$. The joint properties are characterized by parameters $\phi_b = 32°$, $(\alpha_1)_0 = (\alpha_2)_0 = 16°$, $(g_1)^f = (g_2)^f = 10$; for the parameter W_0 three different values have been selected, namely $W_0 = 0.8, 4, 8$ kN cm, as our aim is to study the effects of the wear on joint response.

The results obtained for the same example by Snyman and Martin[9] with the saw-tooth and the spiral models are presented in Figure 11. The diagram in Figure 11(a) demonstrates that the saw-tooth model provides an elastic–perfectly plastic response and the spiral model provides softening behaviour related with the particular asperity shape. In both cases, for the first cycle the elastic behaviour takes place when passing from the right-hand side to the left-hand side of the asperity. The inelastic normal deformation, as shown in Figure 11(b), linearly increases with the inelastic shear deformation in the case of saw-tooth model and reaches a constant value in the case of the spiral model. The results with the hyperbolic model are illustrated in Figure 12. After the elastic phase, a softening behaviour related to the initial wear of asperities occurs; when the value of W_0 decreases i.e. the asperities are weaker, softening becomes more evident until a perfectly brittle behaviour takes place. This prediction well matches with the experimental observations and the results generated by the limited dilatancy model. When the value of $W_0 = \infty$ is assumed, the perfect plastic behaviour occurs similarly as in the case of the saw-tooth model. Along the loading path, the dilatancy increases with increasing shear deformation and the behaviour is similar to that predicted by the saw-tooth asperity model. However,
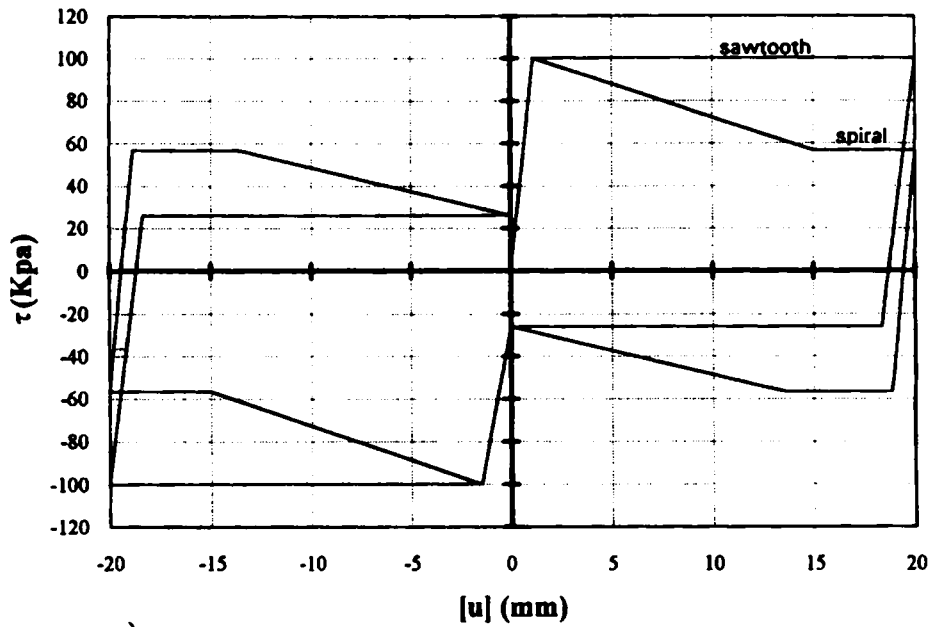
a)
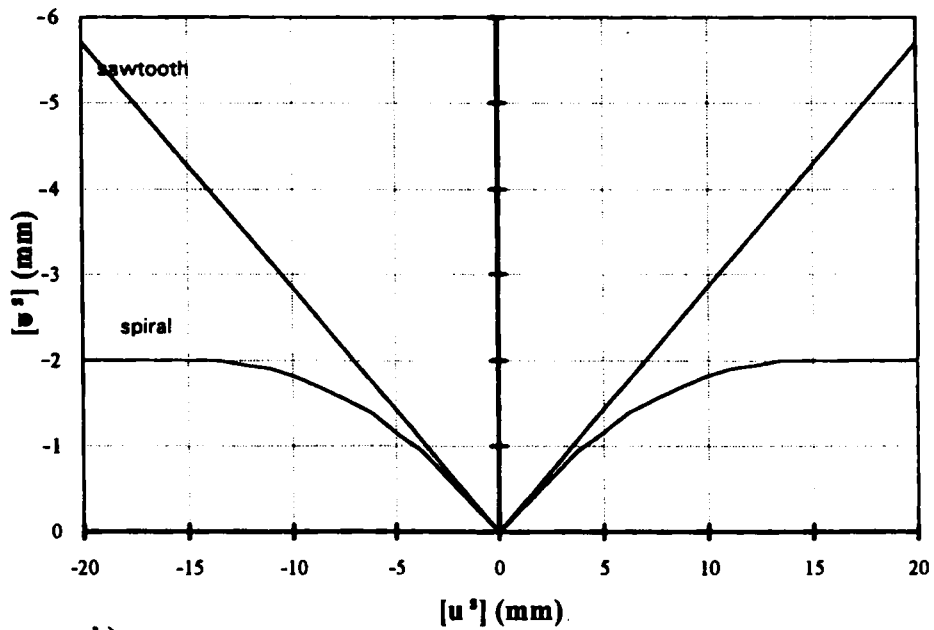
b)

Figure 11. Results for Example 2 obtained with the saw-tooth and spiral large asperity models
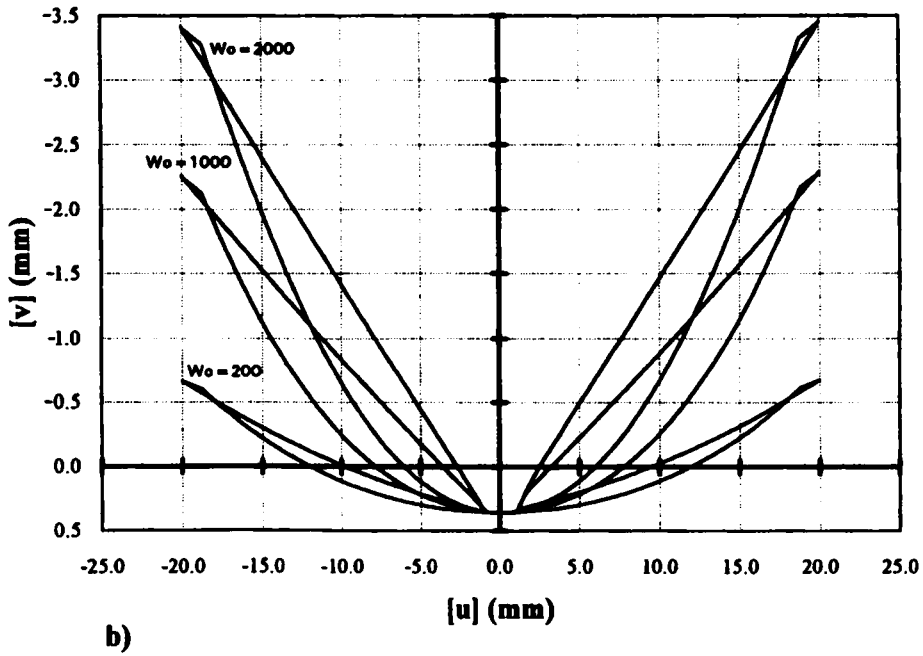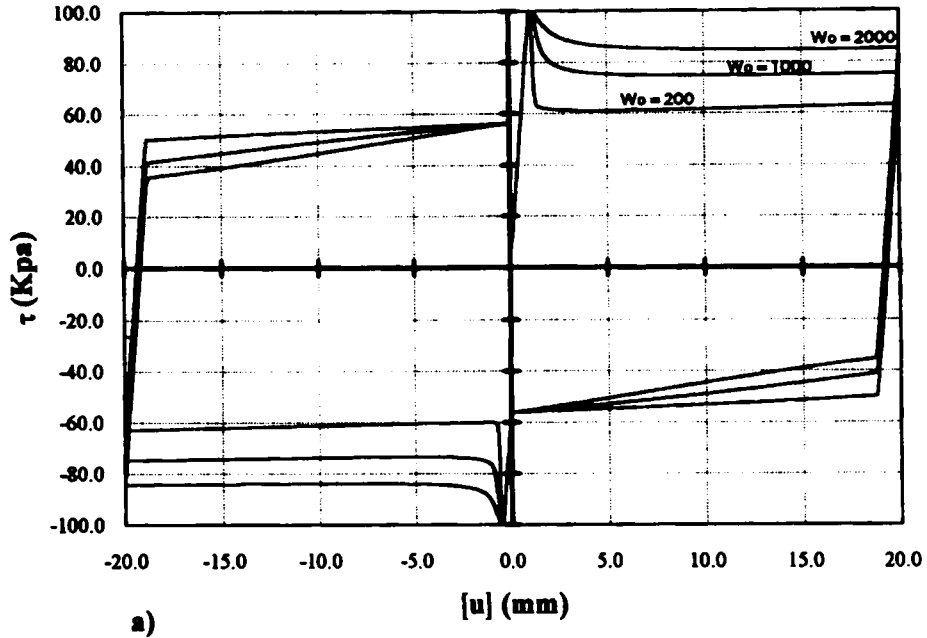
a)

b)

Figure 12. Results for Example 2 obtained with the proposed large asperity model

it changes substantially during unloading process. For decreasing values of W_0 the joint dilatancy decreases.

For this model, a preliminary calibration phase is proposed. In particular, starting from the condition $W_0 = \infty$, the value of g^f, related to the residual effect of the asperities can be identified by comparing the theoretical results with the experimental data for the so-called 'steady cycle', that is the cycle after which there are no more visible variations of the response. The value of W_0 can be determined by observing the softening portion of the loading path. Decreasing the values of W_0 from ∞, we pass from the perfectly plastic response to brittle response through a sequence of different ductile states.

5.3. Example 3. Simulation of Kutter's cyclic shear test

Kutter and Weissbach[18] performed a cyclic directed shear test on a joint in standstone artificially produced. The specimen has the area $495 \, cm^2$ and was subjected to a prescribed tangential displacement history under a constant compressive stress of 2.5 MPa. Three complete cycles were generated and the displacements, in the right direction, varied between 23 and 29 mm and, in the left direction, between 42 and 45 mm.

To describe theoretically the joint behaviour, an interface model 3 cm thick has been used. The values of the elastic compliances adopted for the interface model are: $E = 15 \, MPa \, \nu = 0.3$. The contact surfaces have been characterized by the parameter $\phi_b = 33°$ $(\alpha_1)_0 = 16°$, $(\alpha_2)_0 = 10°$ $(g_1)^f = (g_2)^f = 2$, $W_0^1 = 12 \, kN \, cm$, $W_0^2 = 51 \, kN \, cm$.

The experimental and the theoretical results for the first cycle are shown in Figures 13–15. The model prediction is fairly accurate for the left-hand side of the discontinuity and for the right-hand side some discrepancy can be noted in the pre-peak stage for the stress–displacement diagram. It can be corrected by varying the elastic material parameters constituting the interface and adopting a different exponent p specifying the tangential matrix for slip effects but these possible modifications would affect also the unloading and reloading elastic-slip branches of the diagram where the experimental results exhibit high stiffness. However, for the values of parameters and the slip law used, the predicted deformation response is close to the experimental one. The previous remarks can also be applied here in describing the comparison of predicted and actual dilatancy. For the right-hand side the magnitude of the evaluated dilatancy is larger than that obtained experimentally. In Figure 16 the model predictions for the three cycles are presented. The shear stress–strain and dilatancy curves are in general agreement with the experimental curves. The peak shear stress occurs only in the first cycle and the magnitudes of dilatancy and contraction in subsequent cycle are smaller than those during the preceding cycle. These features are connected with the progressive damage of asperities, simulated in our model using the relation (65) and (51).

5.4. Example 4. Simulation of a shear test on artificial joint

A set of shear tests on artificial joints, replicas of a natural rock specimen, where conducted by Jing[19] at the Lulea University of Technology in order to analyse the shear behaviour of a discontinuity in different direction on the plane of the joint. The artificial specimen was made by concrete and the surface topography was a very close copy of the natural one.

The results obtained from the cyclic test performed on the so-called sample S2, are here used to analyse the response of the mathematical model.
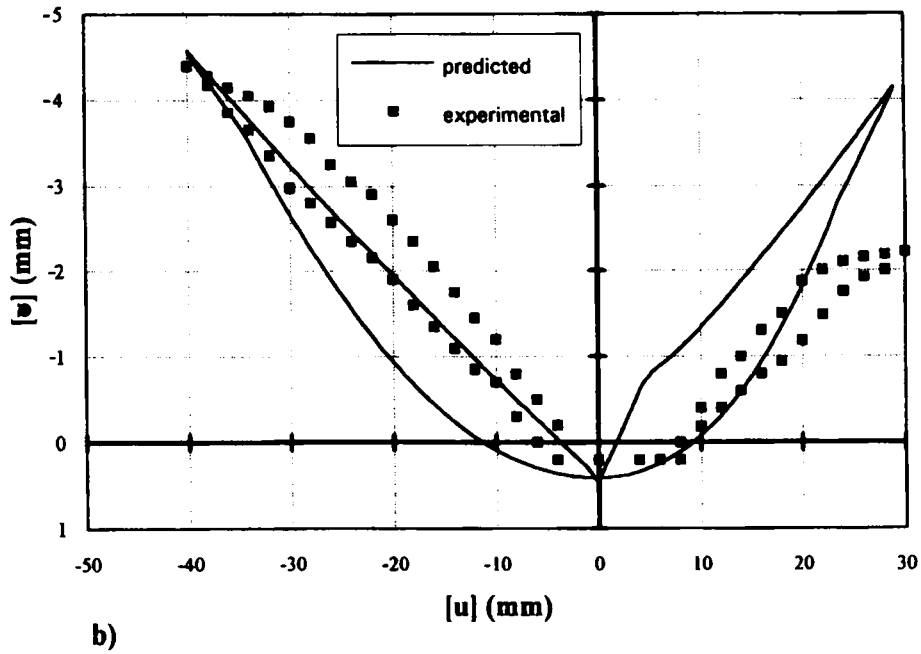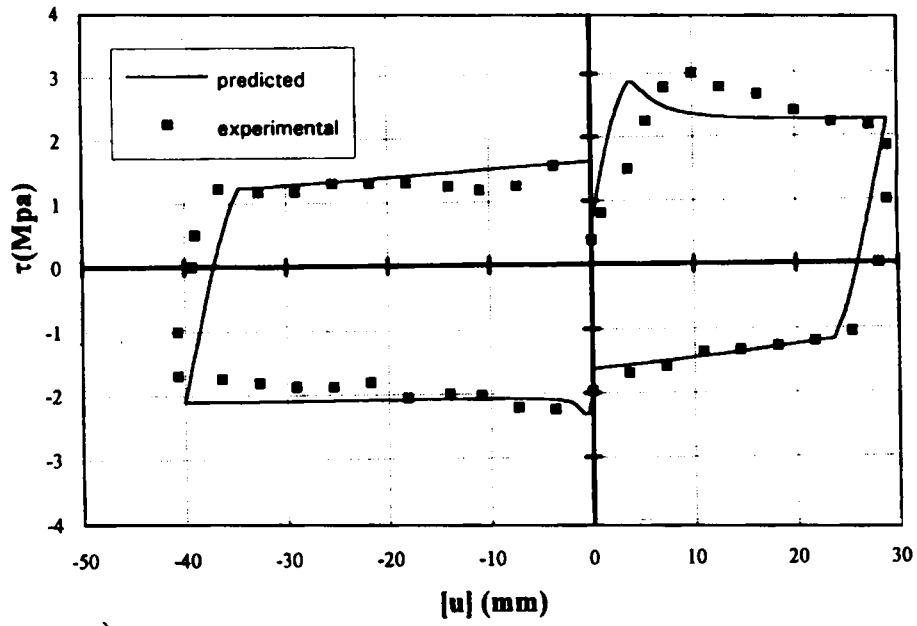
a)

b)

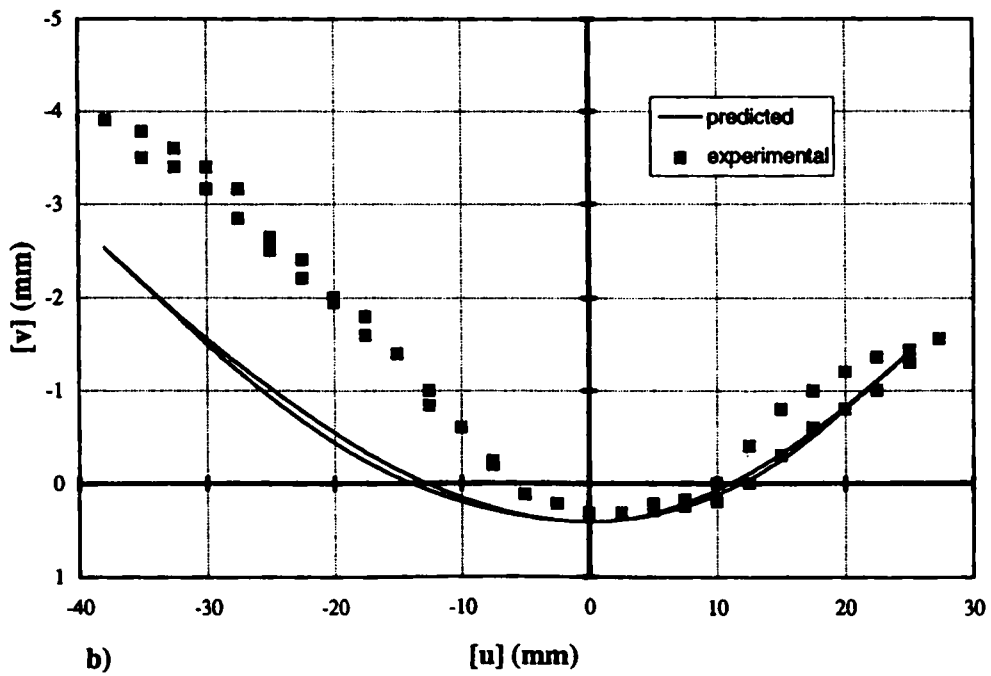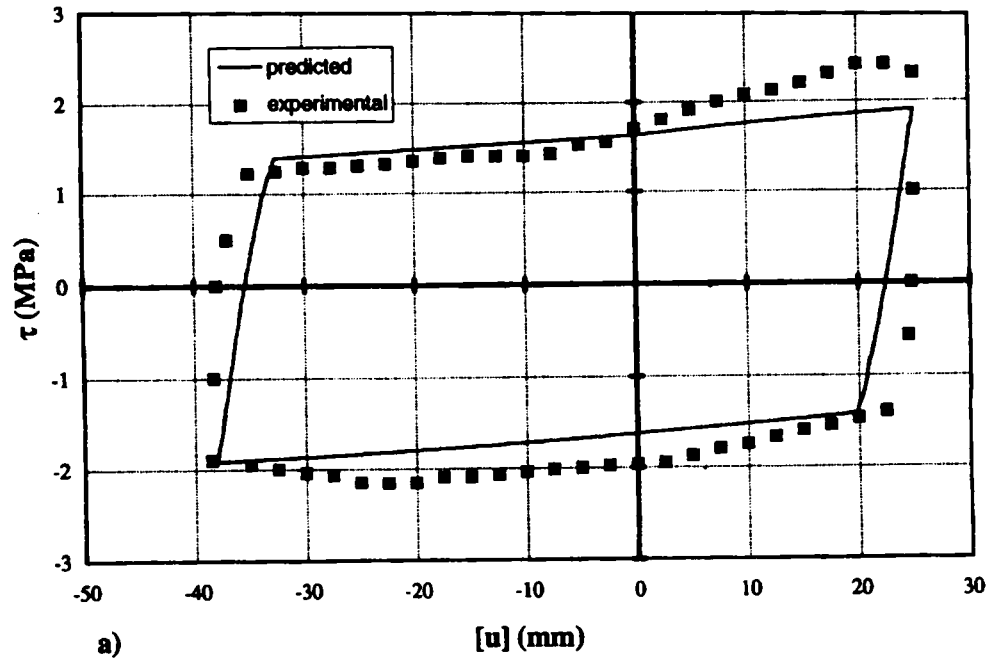Figure 13. Results for the simulation of the first cycle of Kutter's shear test

a)

b)

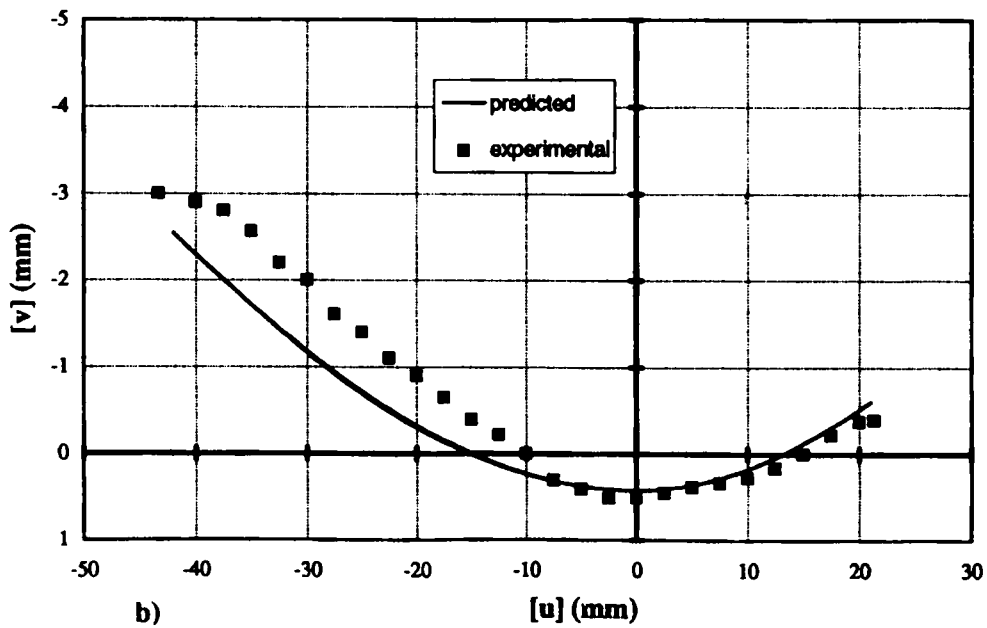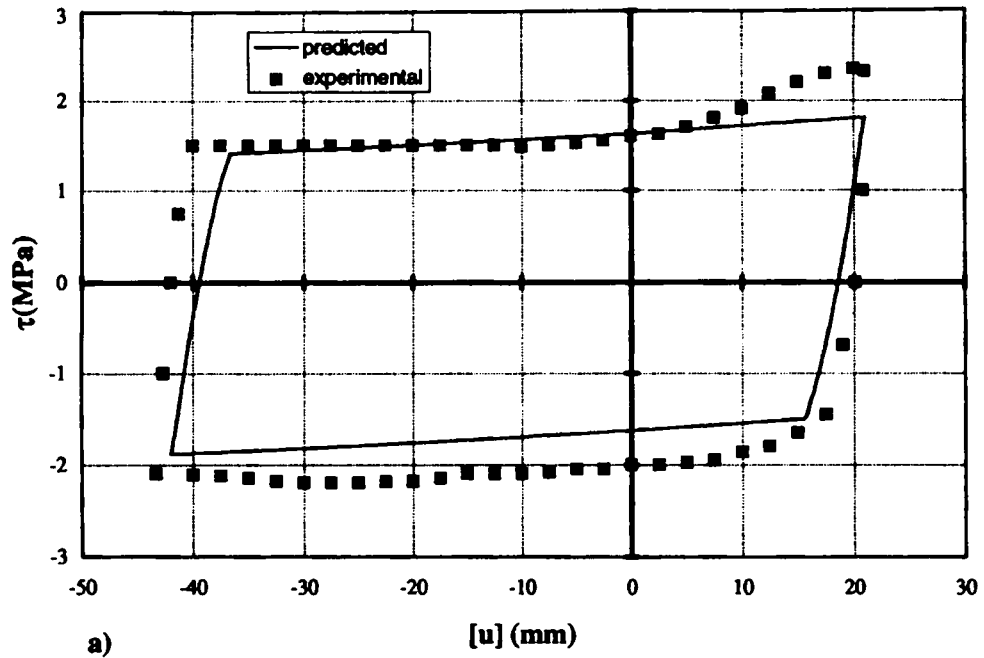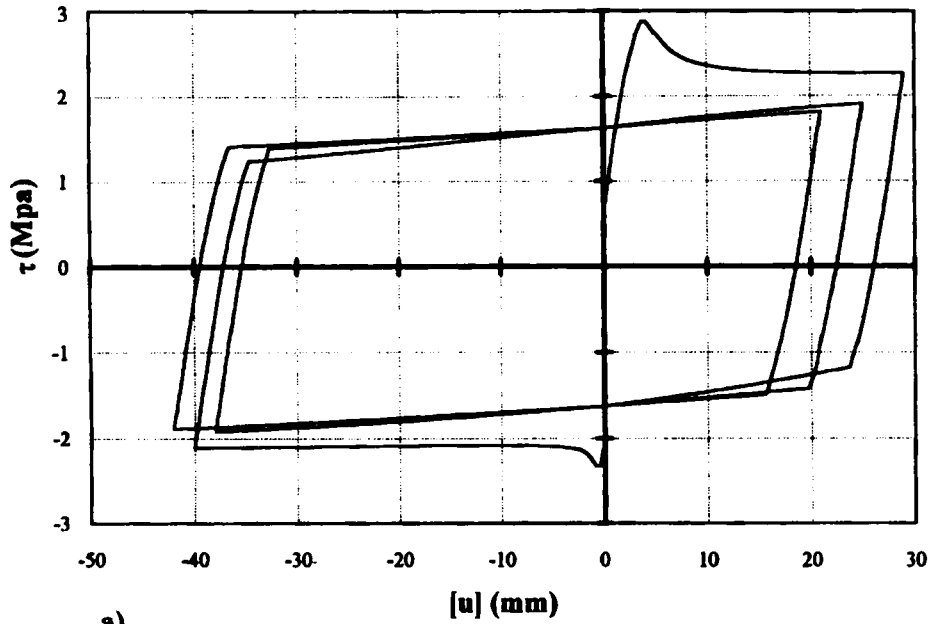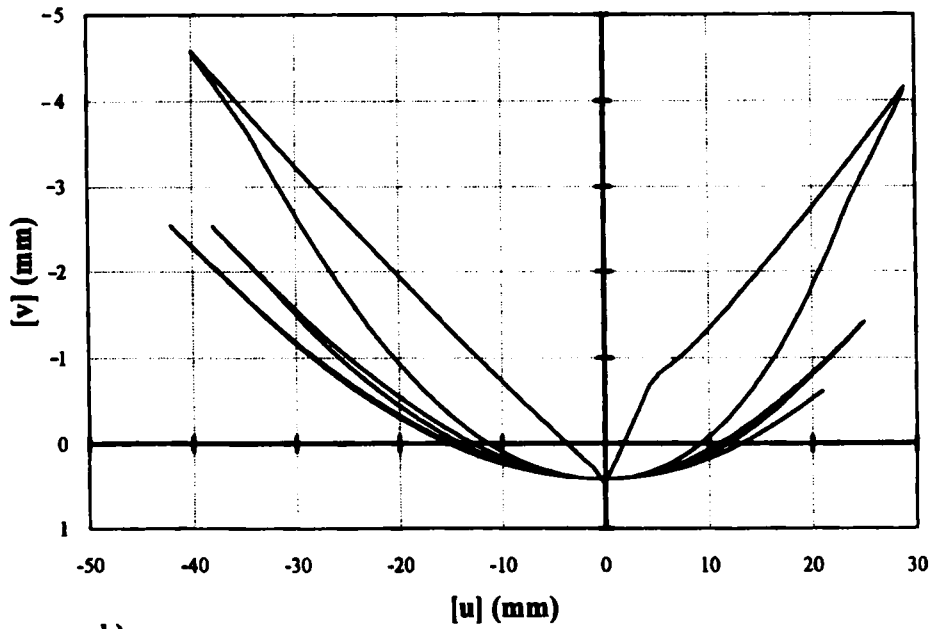Figure 14. Results for the simulation of the second cycle of Kutter's shear test

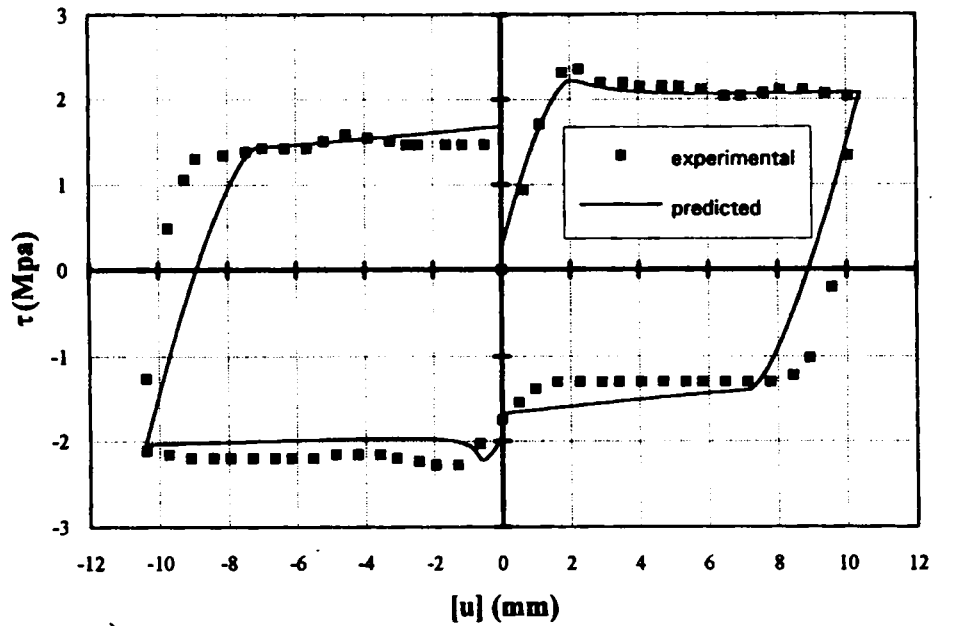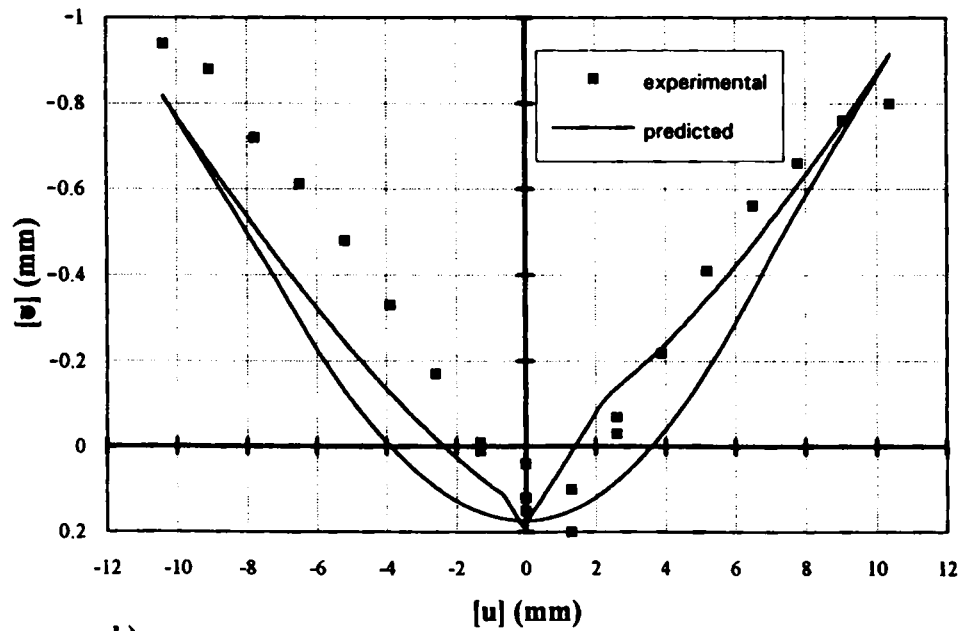Figure 15. Results for the simulation of the third cycle of Kutter's shear test

a)

b)

Figure 16. Results for the simulation of the three cycles of Kutter's shear test

a)

b)

Figure 17. Results for the simulation of the first cycle of Jing's shear test

The specimen was sheared for two consecutive cycles under a constant normal stress $\sigma_n = 2$ MPa and the displacements imposed varied within the range $(-10, +10)$ mm. The experimental values of shear stress and dilatancy, are shown in Figures 17 and 18 for the first and
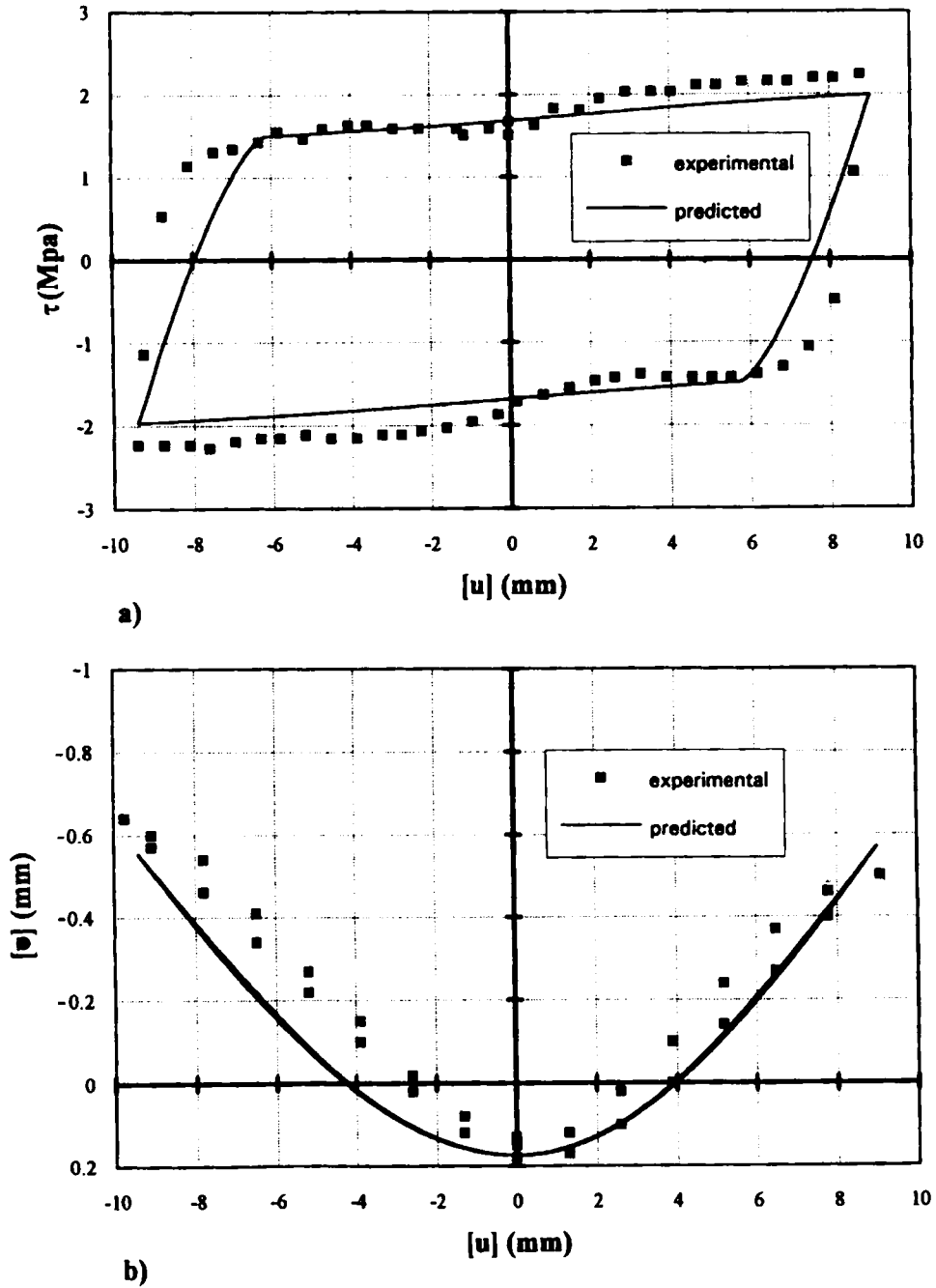
a)

b)

Figure 18. Results for the simulation of the second cycle of Jing's shear test
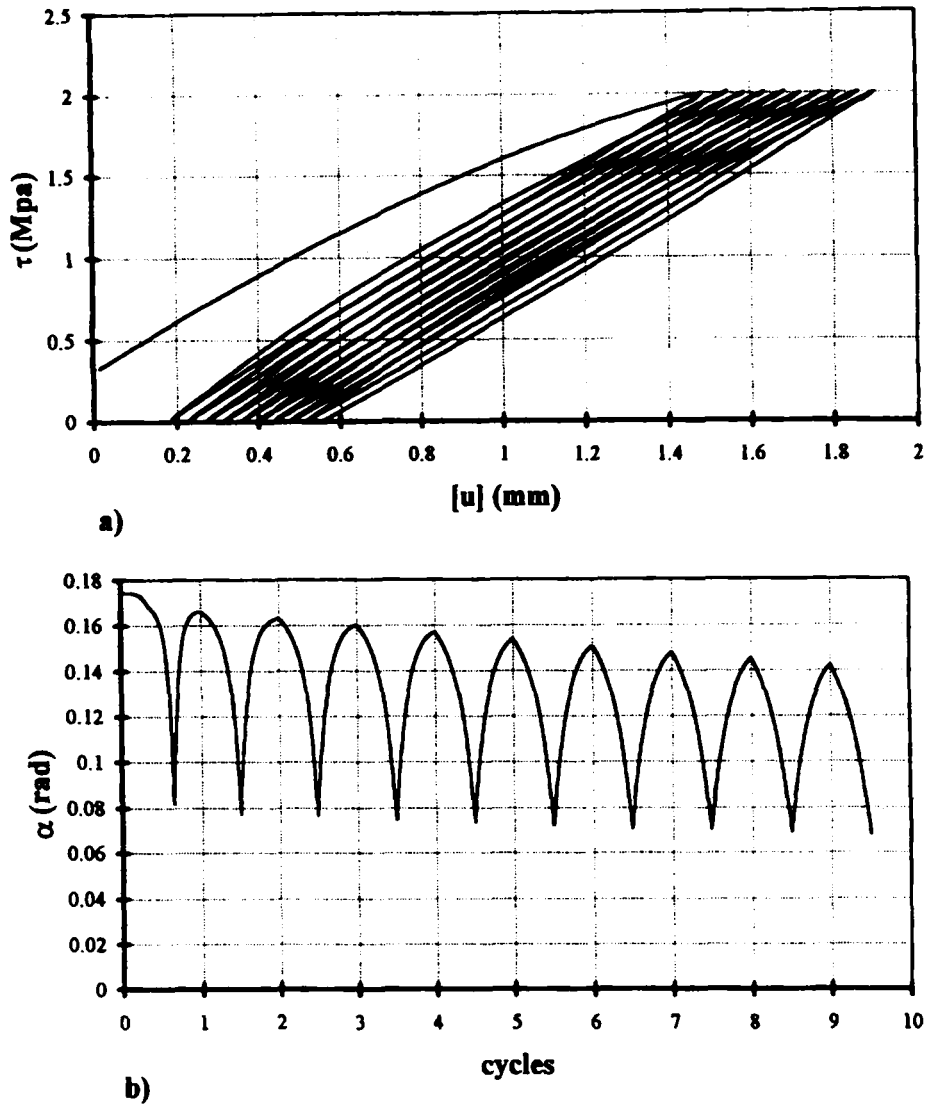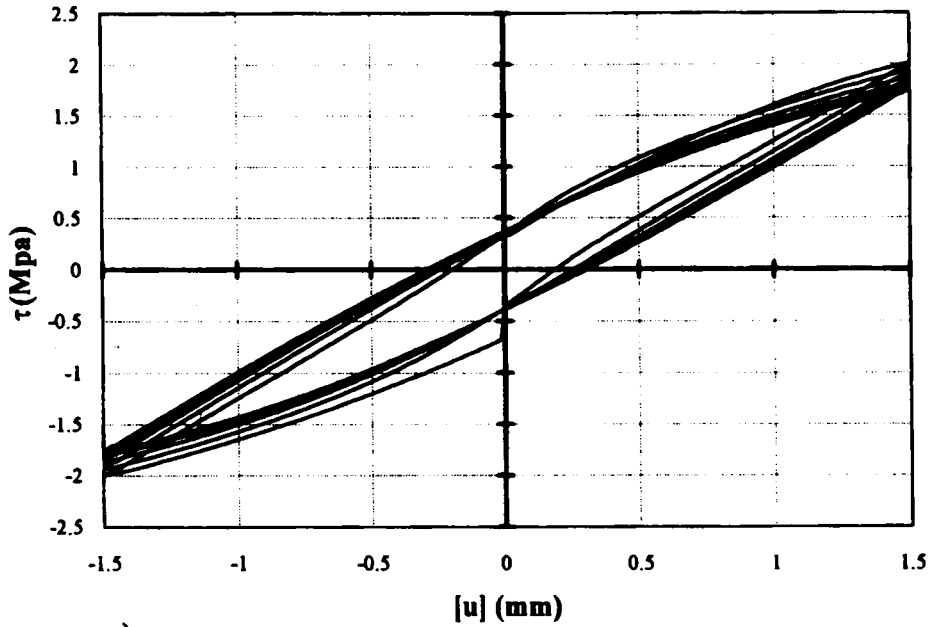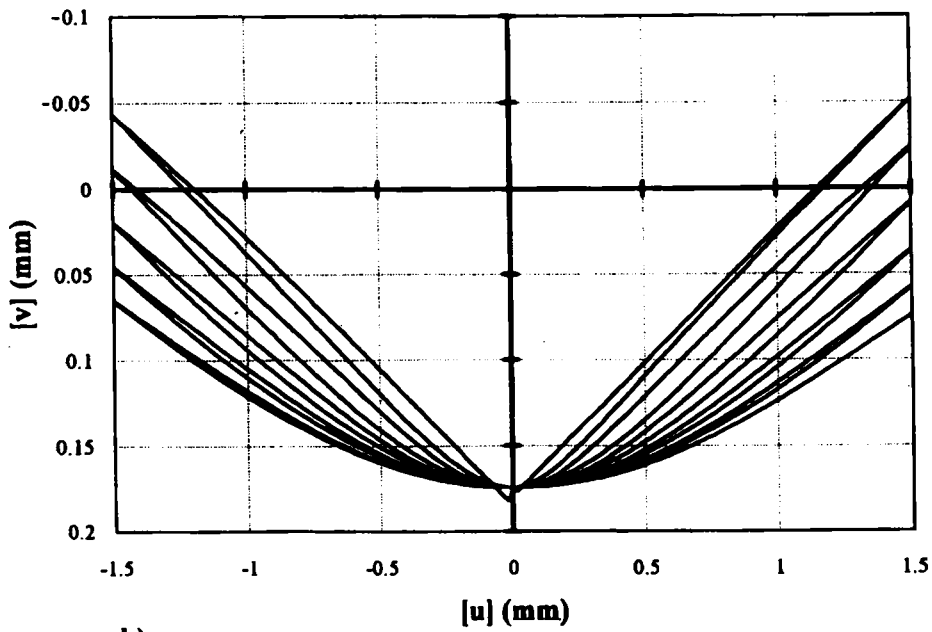
Figure 19. Response of the model imposing load cycles of the same amplitude

second cycle, respectively. In the same diagrams are superimposed the values obtained by the mathematical model using an interface of thickness $h = 5$ mm and with the following values of the material and contact parameters: $E = 30$ MPa $v = 0.35$, $\phi_b = 40°$ $(\alpha_1)_0 = (\alpha_2)_0 = 8°$ $(g_1)^f = 0.35$ $(g_2)^f = 0.4$, $W_0^1 = W_0^2 = 1.25$ kN cm.

The behaviour predicted is very close to the actual one. The shear stress–strain curve in both cycles follows closely the experimental data, though the differences in dilatancy prediction can be noted in the first cycle. In particular, the model predicts different paths for the loading and unloading programs while in the actual response these two paths are almost identical. The other two numerical tests were performed using the same model in order to analyse the mechanical response of the joint for small stress amplitudes. Figure 19 illustrates the results of simulation carried out

a)

b)

Figure 20. Response of the model imposing displacement cycles of the same amplitude
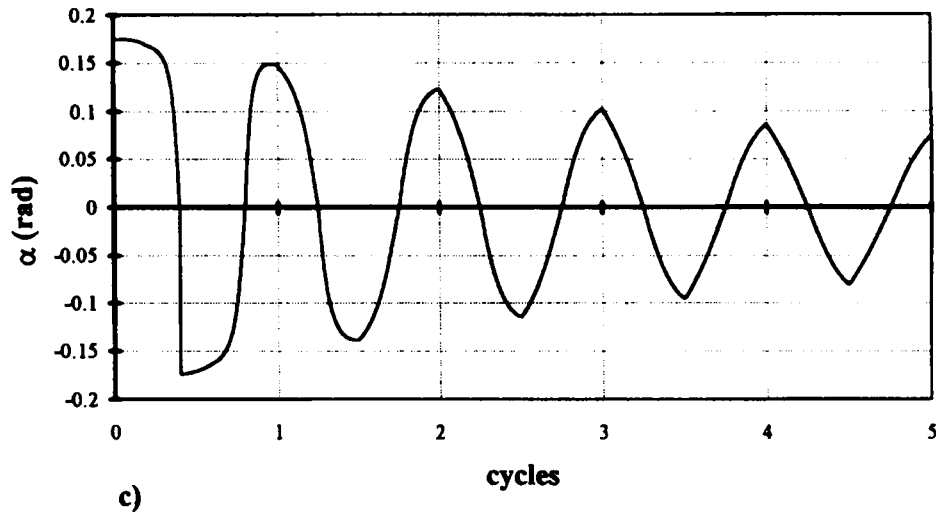
c)

Figure 20. Continued

by imposing subsequent load cycles within the same range 0–2 MPa, i.e. unloading and reloading to the same stress 2 MPa. The right-hand side of the asperity is active only and for each complete cycle a progressive increment of displacement occurs. This phenomenon is associated with the asperity wear due to the frictional dissipation generated in each cycle. In Figure 19(b) the variation of the asperity angles along the deformation path is presented for consecutive cycles. Such asperity evolution of the contact surfaces due to microslip results in the respective stress evolution for strain-induced cycling so that the peak values of shear stress cannot be achieved in consecutive cycles. In the last numerical test, five cycles corresponding to the same imposed displacement amplitude, (−1.5, 1.5) mm, were studied. The diagrams of Figure 20 indicate that all mechanical variables, shear stress, dilatancy and asperity angle, tend to the residual values and the response at the residual state is steady. The hysteretic slip phenomena, theoretically described by the model, are also observed experimentally in contact of metal surfaces, see Courtney et al.[20]

6. CONCLUSIONS

The present paper provides a description of joint or cracked interface response by combining the local asperity slip response with overall sliding along large asperities when the limit friction condition is satisfied. The predicted shear hysteretic response and dilatancy curves are sufficiently close to experimental curves. The model provides good correlation with experiments for a variety of data and loading programs. For very small cyclic strain amplitudes the slip phenomena become predominant and the sliding mode may not occur. On the other hand, for large strain amplitudes, the slip effect may be neglected and only sliding mode could be accounted for. The model provides the possibility to include or neglect one or the other mode of deformation. The application of this model in the analysis of rock mass and masonry structures will be presented separately.

REFERENCES

1. R. E. Goodman, R. L. Taylor and T. L. Brekke, 'A model for the mechanics of jointed rock', *J. Soil Mech. Found. Div. ASCE*, **94**, 637–659 (1968).

2. J. Ghaboussi, E. L. Wilson and J. Isenberg, 'Finite element for rock joints and interfaces', *J. Soil Mech. Found. Div. ASCE*, **99**, 833–848 (1973).

3. M. E. Plesha, 'Constitutive model and finite element procedure for dilatant contact prolems', *J. Eng. Mech. Div. ACSE*, **115**, 345–362 (1987).

4. C. S. Desai and Y. Ma, 'Modelling of joints and interfaces using the disturbed state concept', *Int. J. Num. Anal. Methods Geomech.*, **16**, 623–653 (1992).

5. N. Navayogarajah, C. S. Desai and P. D. Kiousis, 'Hierarchical single surface model for static and cyclic behaviour of interfaces', *J. Soil Mech. Found. Div. ASCE*, **98**, 399–422 (1972).

6. R. E. Goodman and J. Dobois, 'Duplication of dilatancy in analysis of jointed rocks'. *J. Soil Mech. Found. Div. ASCE*, **98**, 399–422 (1972).

7. F. D. Patton, 'Multiple modes of shear failure in rock', *Proc. 1st Congress ISRM*, Vol. 1, Lisbon, 1966, pp. 509–513.

8. N. R. Barton, A. C. Lumsden and S. C. Bandis, 'Fundamentals of rock joint behaviour', *Int. J. Rock Mech. Min. Sci. Geomech., Abstr.*, **20**, 249–268 (1983).

9. M. E. Plesha, 'Constitutive models for rock discontinuities and surface degradation'. *Int. J. Numer. Anal. Methods Geomech.*, **11**, 345–362 (1987).

10. M. F. Snyman and J. B. Martin, 'A consistent formulation of a dilatant interface element', *Int. J. Numer. Anal. Methods Geomech.*, **16**, 493–527 (1992).

11. R. Michalowski and Z. Mroz, 'Associated and non associated sliding rules in contact friction problems' *Arch. Mech.* **30**, 259–276 (1978).

12. Z. Mroz and S. Stupkiewicz, 'An anisotropic friction and wear model'. *Int. J. Solids Struct.*, **31**, 1113–1131 (1994).

13. H. R. Lofti and P. B. Shing, 'Interface model applied to fracture of masonry structures', *J. Struct Engg. ASCE*, **120**, 63–80 (1994).

14. Z. Mroz and A. Jarzebowski, 'Phenomenological model of contact slip', *Acta Mech.*, **102**, 59–72, (1994).

15. A. Jarzebowski and Z. Mroz, 'On slip and memory rules in elastic friction contact problems', *Acta Mech.*, **102**, 199–216 (1994).

16. R. D. Mindlin and H. Deresiewicz, 'Elastic spheres in contact under varying oblique forces', *J. Appl. Mech.*, **75**, 327–344 (1953).

17. R. Dobry, T.-T. Ng, E. Petrakis and E. Seridi, 'General model for contact law between two rough spheres', *J. Eng. Mech. ASCE.*, **117**, 1365–1381 (1991).

18. N. Barton, S. Bandis and K. Bakhtar, 'Strength, deformation and conductivity coupling of rock joints', *Int. J. Rock Mech. Min. Sci. Geomech. Abstr.*, **22**, 121–140 (1985).

19. H. K. Kutter, G. Weissbach and K. Bakhtar, 'Der Einfluss von Verformungs- und Belastungsgeschichte auf den Scherwiderstand von Gesteinskluften unter besonderer Berucksichtigung der Mylonitbildung', *Final Report, DFG Research Project Ku 361/2/4*, 1980.

20. L. Jing, Numerical modelling of jointed rock masses by distinct element method for two, and three-dimensional problems, *Doctoral Thesis*, Lulea University of Technology, 1990.

21. J. S. Courtney-Pratt and E. Eisner, 'The effect of a tangential force on the contact of metallic bodies', *Proc. Roy. Soc. London A.*, **238**, 529–550